ADVANCED MATERIALS
www.advmat.de

www.MaterialsViews.com

Infrared Colloidal Quantum Dots for Photovoltaics: Fundamentals and Recent Progress

*Jiang Tang and Edward H. Sargent**

Colloidal quantum dots (CQDs) are solution-processed semiconductors of interest in low-cost photovoltaics. Tuning of the bandgap of CQD films via the quantum size effect enables customization of solar cells' absorption profile to match the sun's broad visible- and infrared-containing spectrum reaching the earth. Here we review recent progress in the realization of low-cost, efficient solar cells based on CQDs. We focus in particular on CQD materials and approaches that provide both infrared and visible-wavelength solar power conversion CQD photovoltaics now exceed 5% solar power conversion efficiency, achieved by the introduction of a new architecture, the depleted-heterojunction CQD solar cell, that jointly maximizes current, voltage, and fill factor. CQD solar cells have also seen major progress in materials processing for stability, recently achieving extended operating lifetimes in an air ambient. We summarize progress both in device operation and also in gaining new insights into materials properties and processing – including new electrical contact materials and deposition techniques, as well as CQD synthesis, surface treatments, film-forming technologies – that underpin these rapid advances.

1. Introduction

Single-crystal materials such as silicon and epitaxial III-V compound semiconductors have led to remarkable solar photovoltaic power conversion efficiencies in the range of 20–41.4%.[1,2] For their high efficiencies, these devices rely on the efficient matching of the light absorption spectrum to that of the sun's power reaching the earth; combined with the excellent electronic transport properties of crystalline semiconductors.

In parallel, low-cost, low-energy-consumption means of producing solar cells – often using solution-processing and roll-to-roll fabrication[3] – have emerged in recent years. Organic and polymer photovoltaics represent a particularly promising example of these low-cost devices. The organics have recently reached published AM1.5 power conversion efficiencies of 6.8%[4] – a particularly impressive achievement in view of the constraints on these devices' maximum theoretical efficiencies including their limited spectral absorption and considerable exciton dissociation energy.[5]

There is considerable interest in photovoltaic technologies that suffer no compromise between the desired high efficiency and equally important low cost.

The present review focuses on emerging solar cell technologies that are:

(1) solution-processed;
(2) fabricated at 200 °C and below;
(3) capable of absorbing the sun's entire visible, near infrared, and short-wavelength infrared;
(4) significantly spectrally tuned via the quantum size effect, empowering a single material strategy to create the different-bandgap layers required to produce stacked multi-junction solar cells.

Colloidal quantum dots (CQDs), synthesized in the solution phase and may be coated on substrates (including flexible ones) using drop-casting,[6] spin-coating[7] and ink-jet printing,[8–10] have demonstrated many potential applications such as light emitting diodes.[11–13] In this research progress report, we focus in particular on infrared CQDs for photovoltaic applications. The materials that have seen the most intensive recent investigation – PbS and PbSe CQDs – possess bulk bandgaps that lie to the red of even the longest-wavelength junction required in multi-junction cells. Their large Bohr exciton radius allows wide tunability, even producing bandgaps that cut off at the red edge of the visible. As a consequence, these materials offer a single, binary-composition, strategy to produce any and all of the junctions needed in triple-junction photovoltaics.

We begin with a discussion of material selection in CQD photovoltaics. We proceed to review briefly the fundamentals of p-n junctions and solar cell operation. We then introduce the experimental tools used to characterize the electrical properties of CQD films. We follow with a review of the latest understanding of carrier transport, surface passivation, doping, and dielectric constant in CQD films. We close with a detailed account of the latest research progress in performance, materials processing, and stability of CQD solar cells and a perspective on some of the many key questions and opportunities remaining open in the field.

Prof. E. H. Sargent
Department of Electrical and Computer Engineering
University of Toronto
10 King's College Road, Toronto, Ontario M5S 3G4, Canada
E-mail: ted.sargent@utoronto.ca
J. Tang
Department of Materials Science and Engineering
University of Toronto
184 College Street, Toronto, Ontario M5S 3E4, Canada

DOI: 10.1002/adma.201001491

2. Infrared CQDs for the Full Absorption of Solar Spectrum

2.1. Bandgap Engineering for the Broadband Solar Spectrum Match

Before it reaches the earth's surface, the black body radiation (T = 5762 K) from sun is attenuated by the ozone, moisture, carbon dioxide, dust and other components in the atmosphere. AM1.5G (air mass 1.5 global includes both direct and diffusive radiation) is thus adopted as the standard spectrum for testing. The integrated power density of AM1.5G is 100 mW cm^{-2} with the spectral intensity distribution matching that of sunlight at the earth's surface at an incident angle of 48.2°. As shown in **Figure 1A**, AM1.5G is a broadband spectrum spanning from ~280 nm in the ultraviolet to ~4000 nm mid-infrared region. Half of the integrated power resides in the infrared spectral region.

Figure 1A includes the absorption onset of 15 typical bulk semiconductors with respect to the AM1.5G spectrum. In inorganic semiconductors, the absorption coefficient generally increases as the photon energy is increased starting from the semiconductor's band edge, in contrast with many organics whose absorption spectra peak as a result of the well-defined HOMO-LUMO transition.[14] Low-bandgap materials absorb more light and produce large current at the cost of a low voltage; in contrast, large-bandgap materials output high voltage but low current due to their limited absorption. As a consequence, the balance between voltage and current necessitates an optimal choice of bandgap in the range of 1.1–1.4 eV in order to yield the best power conversion efficiency in a single-junction solar cell. Bulk Si, InP and $CuInSe_2$ have the optimal bandgaps, while bulk PbS, InAs and PbSe are not suitable for photovoltaic application.

One way to tune the bandgap of semiconductor is to manipulate its composition. According to Vegard's law,[15] the bandgap of an alloyed semiconductor is approximately equal to the compositionally-weighted average of the bandgaps of the constituent semiconductors. Ternary and quaternary compounds such as InGaP, $CuInGaSe_2$ and $CuZnSnS_2$ provide stoichiometry-tuned absorber materials for efficient photovoltaics.

Quantum confinement provides a promising alternative for bandgap engineering without relying on ternary and quaternary stoichiometric tuning. Decreasing the size of particles

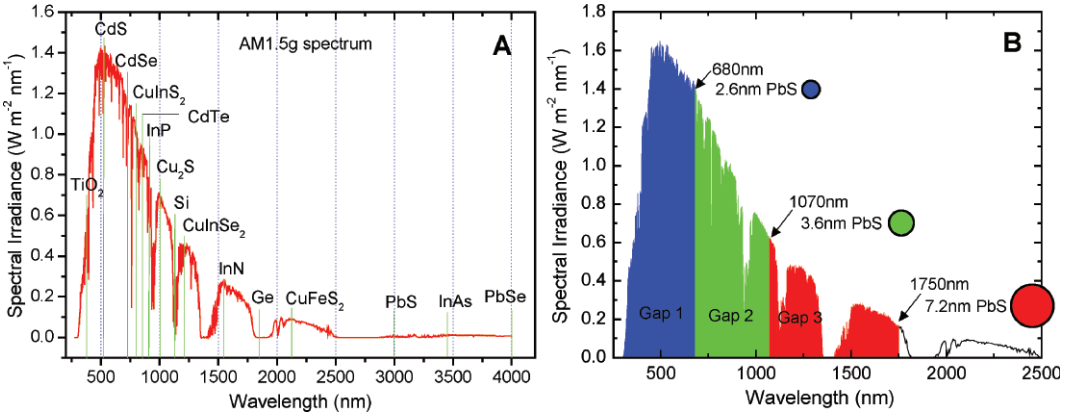

Figure 1. (A) AM1.5G solar spectrum from ASTM G173–03 reference spectra. The bandgaps for some common bulk semiconductors are: TiO_2 3.3 eV; CdS 2.5 eV; CdSe 1.7 eV; $CuInS_2$ 1.54 eV; CdTe 1.5 eV; InP 1.34 eV; Cu_2S 1.21 eV; Si 1.12 eV; $CuInSe_2$ 1.0 eV; InN 0.8 eV; Ge 0.66 eV; $CuFeS_2$ 0.6 eV; PbS 0.41 eV; InAs 0.35 eV and PbSe 0.28 eV. (B) Concept of using PbS CQDs with different sizes to build a triple-junction tandem solar cell.

Jiang Tang is currently a Ph.D student in Prof. Edward H. Sargent's group at University of Toronto. He received his BS from University of Science and Technology of China in 2003 and his MS from Changchun Institute of Applied Chemistry, Chinese Academy of Sciences in 2006. His research focused on the synthesis of semiconductor nanomaterials and their application for photodetector and photovoltaics, with special emphasis on stable and efficient PbS colloidal quantum dot solar cells.

Prof. Edward H. Sargent holds the Canada Research Chair in Nanotechnology in the Edward S. Rogers Sr. Department of Electrical and Computer Engineering at the University of Toronto. He is a KAUST Investigator and a Fellow of the AAAS. He received the PhD in Electrical and Computer Engineering from the, University of Toronto in 1998 and his B.Sc.Eng. from Queen's University in 1995.

to less than their Bohr radius results in confinement of electron and hole wavefunctions and a significant increase in bandgap.[16,17] This strategy enables use of low-bandgap binary compound semiconductors such as PbS and PbSe for photovoltaic application.

We illustrate the quantitative aspects of quantum size effect tuning for the case of PbS (The numbers are similar for the case of PbSe). The Bohr radius of excitons in PbS is 18 nm. By controlling the size of PbS CQDs in synthesis, the absorption onset can be tuned from 3000 nm to ~600 nm.[18] In the case of a single-junction device having optimal bandgap circa E_g = 1.1 eV, PbS CQDs of diameter ~3.5 nm are desired. A triple-junction solar cell may also be achieved within a single material system:[19]

the first (top) layer is composed of smallest PbS CQDs with diameters of 2.6 nm and absorption onset 680 nm;
the second layer is composed of PbS CQDs with diameters of 3.6 nm and absorption onset 1070 nm;
the bottom layer is composed of PbS CQDs with diameters of 7.2 nm and absorption onset 1750 nm.
The resultant distribution of spectral absorbance is illustrated schematically in Figure 1B.

The desire for solution-processing, combined with the need for absorption of the majority of the sun's broad solar spectrum, motivates interest in infrared colloidal nanoparticles. Since InP, CdSe, CdTe have bulk bandgaps in the near infrared, quantum confinement generally tunes them into the visible. They may be of interest in one junction in a multi-junction cell, but are not materials that offer to span the entire multi-junction stack.[19] Si, Cu_2S, $CuInS_2$, $CuInGaSe_2$ and $CuZnInS_2$, having small Bohr exciton radii, generally preserve their bulk properties. Here we focus therefore on photovoltaics based on infrared CQDs that offer wide tuning across the solar spectrum based on a dramatic range of quantum confinement. These materials hold great potential for low-cost, high efficiency photovoltaics. Intensive effort in these materials in the past five years has also raised a number of important fundamental and applied questions that merit review.

2.2. Light Absorption in CQD Film

Light absorption may be described using the Beer-Lambert law:

$$I = I_0 e^{-\alpha(h\upsilon)l} \quad (1)$$

where I,I_0, $\alpha(h\upsilon)$ and l are the transmitted light intensity, incident light intensity, absorption coefficient, and film thickness, respectively. Indirect-bandgap semiconductors offer weak absorption coefficient because their absorption relies on a multi-particle interaction that includes a phonon. Direct-bandgap semiconductors offer much stronger absorption coefficient, providing α of 10^4 cm^{-1} and above. Such a strong absorption enables reduced materials consumption and enables the realization of efficient devices based on materials having modest transport lengths.

The absorption coefficient of CQDs is of crucial importance in engineering films of suitable thicknesses to enable efficient photovoltaics. Studies on CQDs dispersed in solution provide a basis for interpreting film-based results.[20,21] **Figure 2** provides

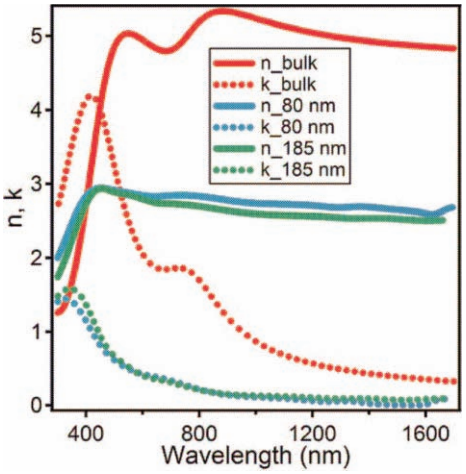

Figure 2. The optical constants of PbSe CQD films of two different thicknesses (80 and 185 nm) relative to the values for bulk PbSe. Data were obtained from ellipsometry measurements. Reproduced with permission[22] Copyright 2009, American Chemical Society.

the refractive index n and extinction coefficient k for typical PbSe CQD films and provides a comparison with bulk PbSe.[22] For this study, PbSe CQDs having an excitonic peak at 1686 nm were treated using 1,2-ethanedithiol (EDT). At short wavelengths, the absorption coefficient was ~5 times lower than that of bulk PbSe, suggestive of 20% by volume of CQDs within the film.[21] Optical penetration depths were estimated to be ~20 nm for 400 nm wavelength photons and ~500 nm for 1700 nm wavelength photons. Similar optical penetration depths have been obtained for PbS CQD films having a similar quantum-confined bandgap.[23]

Many CQD photovoltaics employ a reflective back contact. To achieve 90% absorption of incident photons in a double-pass fashion, and use the absorption coefficient for photons with bandgap wavelength (most weakly-absorbed), simple calculation suggests that about 1 μm worth of CQD film is required, which is much thinner than indirect-gap devices such as Si (typically 100 μm is required).

3. Semiconductor Solar Cell Fundamentals

3.1. Fundamentals of P-N Junction

To provide a framework for investigation and optimization of CQD materials and devices summarized herein, we begin with an introduction to the operation of semiconductor p-n junction devices. We first point out evident deviations of CQD films from the homogeneous bulk film described by the canonical semiconductor theory and justify our pursuit of this first-order, highly simplified model notwithstanding:

1) Strong electron interactions in bulk semiconductor solids and periodic crystal structures result in the formation of bands of delocalized carriers; whereas in semiconductor CQD films, CQDs are surrounded by an insulting matrix material, typically organic ligands, and hence carriers are largely confined to the CQDs. Transport in these films occurs mainly through

tunneling or hopping. Carrier transport can be described in both cases by an average velocity – thus a time to transit a depletion region or a quasi-neutral region – and this simple consideration underpins many general concepts such as characteristic drift and diffusion length scales of major importance to understanding the performance of junction-based devices.

2) CQD films incorporate quantum dots that results in a large internal surface area and may also produce fluctuations in doping and trap state distributions across the film. Spatially-averaged doping and defect densities may nonetheless be applied over macroscopic (many tens of quantum dots) volumes. Such volumes correspond to the measured length scales of depletion regions, diffusion lengths, and drift lengths in these films, justifying their judicious use as helpful simplifying approximations.

When a p-type and a n-type semiconductor are brought together, diffusion of majority carriers leads to the establishment of depletion region. The width of this region, W, is:

$$W = \left[\frac{2\varepsilon kT}{q^2}\left(\ln\left(\frac{N_A N_D}{n_i^2}\right)\left(\frac{1}{N_A}+\frac{1}{N_D}\right)\right)\right]^{1/2} \quad (2)$$

where ε, k, T, q, n_i, N_A and N_D are the permittivity, Boltzmann's constant, temperature, elementary charge, intrinsic carrier density, acceptor density and donor density, respectively. Permittivity ε is the product of dielectric constant (or relative permittivity) ε_m and the permittivity of vacuum ε_0. Depletion region is not equally distributed on both side, but rather spread wider on the relatively less doped region based on:

$$x_{p0} = \frac{W}{1+N_A/N_D}x_{n0} = \frac{W}{1+N_D/N_A} \quad (3)$$

x_{p0} and x_{n0} is the depletion region width in the p-side and n-side, respectively.

V_0, the built-in potential, reflects the potential change within the depletion region. It is dependent on the doping density:

$$V_0 = \frac{kT}{q}\ln\left(\frac{N_A N_D}{n_i^2}\right) \quad (4)$$

Carrier transport relies on drift in the depletion region and diffusion in the quasi-neutral region, as indicated in **Figure 3A**. The drift length l_{drift} depends on built-in field E, carrier mobility μ and carrier lifetime τ:

$$l_{drift} = \mu E\tau \quad (5)$$

The carrier diffusion length $l_{diffusion}$ is calculated as:

$$l_{diffusion} = \sqrt{D\tau} \quad (6)$$

Diffusion coefficient D and carrier mobility μ are related by the Einstein relation:

$$\frac{D}{\mu} = \frac{kT}{q} \quad (7)$$

Under illumination, photogenerated carriers in the depletion region are swept by the built-in field to the edges of the depletion region. These carriers, as well as carriers generated

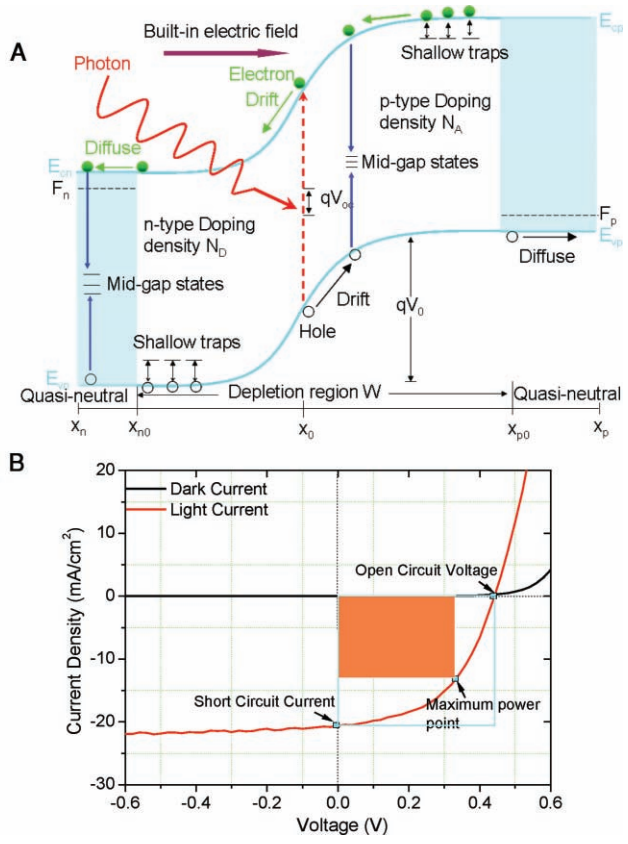

Figure 3. (A) Schematic diagram of a p-n junction. qV_{oc} is the difference between the quasi-Fermi level F_n of electrons in the n-type material and quasi-Fermi level F_p of holes in the p-type material under illumination. Mid-gap states and shallow traps are present in both the p- and the n-type materials. Shallow traps capture and/or release free carriers to the valence/conduction band through thermal activation. Mid-gap states act as catalytic sites for electrons and holes recombination. (B) *J–V* characteristic of a solar cell in the dark and under 1-sun illumination. The area of the orange rectangle represents the maximum power output, the product of the optimally-chosen operating current and voltage.

in the quasi-neutral region, are required to diffuse across the quasi-neutral region to their respective collecting electrodes. Mid-gap states, also known as recombination centers, provide undesired nonradiative pathways for the loss of carriers prior to their successful extraction (Figure 3A). Shallow traps play a much less deleterious role, extending excited state lifetime at the price of lowered mobility, typically keeping the mobility and lifetime product unchanged compared to the trap-free case.

While the preceding discussion ostensibly focused on homojunctions, Schottky (metal-semiconductor) contacts and heterojunctions function similarly. For Schottky contacts, band-bending occurs at the metal-semiconductor interface. The metal contact can be viewed as heavily doped ($N > 10^{21}$ cm^{-3}) semiconductor which, per Equations 2, 3, indicates that the entire depletion region falls on the semiconductor side of the junction. Schottky devices are thus sometimes referred to as single-sided p-n junctions. In the case of heterojunctions, the difference in the Fermi energies across the semiconductor-semiconductor junction produces a depletion region and thus a driving force for the separation of photogenerated carriers as

described above. Differences in electron affinity and ionization potential provide for additional discontinuities in conduction and valence bands across the interface that – ideally – should promote the donation of one carrier (e.g. electrons) to the acceptor side, and block the egress of the other type of charge carrier (e.g. holes).

3.2. Fundamentals of Solar Cells

Figure 3B shows the current density as a function of voltage (*J*–*V*) characteristic of a solar cell in the dark and under illumination. The dark current shows rectification, characteristic of the diode nature of a solar cell. Under illumination, photogenerated carriers shift the *J*–*V* curve downward into the fourth quadrant. The power conversion efficiency η is given by:

$$\eta = \frac{V_{max} J_{max}}{P_{inc}} = \frac{V_{oc} J_{sc} FF}{P_{inc}} \quad (8)$$

where V_{max} and J_{max} are the voltage and current density at the maximum power point, P_{inc} is the incident light intensity, V_{oc} is the open-circuit voltage, J_{sc} is the short-circuit current density and *FF* is the fill factor.

The short-circuit current density J_{sc} is the maximum number of photogenerated carriers per unit area that are extracted from the solar cell. J_{sc} depends on illumination intensity, the total absorbance of the solar cell and its match to the solar spectrum, and recombination losses prior to extraction. J_{sc} can also be obtained by integrating the external quantum efficiency (EQE) or incident-photon-to-electron conversion efficiency (IPCE) with the standard AM1.5G spectrum.

The open circuit voltage V_{oc} is the maximum voltage that a solar cell can generate. V_{oc} reflects the difference between the quasi-Fermi level of electrons F_n in the n-type material and the quasi-Fermi level of holes F_p in the p-type material. V_{oc} and J_{sc} are related with one another, and with the reverse saturation current density J_0, as follows:

$$V_{oc} = \frac{kT}{q} \ln \frac{J_{sc} + J_0}{J_0} \approx \frac{kT}{q} \ln \frac{J_{sc}}{J_0} \quad (9)$$

This mandates a low reverse saturation current density J_0, requiring low recombination in the quasi-neutral region and a highly rectifying diode.

In real photovoltaic devices, parasitic series resistance R_s and shunt resistance R_{sh} also need to be considered. The following equation describes the *J*–*V* characteristics of a realistic solar cell:

$$J = J'_{sc} - J_0 \left[\exp\left(\frac{q(V + JR_s)}{A_0 kT} \right) - 1 \right] - \frac{V + JR_s}{R_{sh}} \quad (10)$$

where J_{sc}' is the short-circuit current density when series resistance is zero and the shunt resistance is infinite; A_0 is the diode ideality factor and it typically has a value between 1 and 2. As can be seen in Equation 10, series resistance R_s reduces J_{sc} but has no effect on V_{oc}, while shunt resistance R_{sh} has no effect on J_{sc} but reduces the V_{oc}. R_s is the sum of film resistance, electrode resistance and the contact resistance between the film and the electrode. R_{sh} is mainly associated with carrier recombination loss. In addition, *FF* is also related to R_s and R_{sh}: large R_{sh} and small R_s leads to device with good *FF*. In a word, maximized R_{sh} and minimized R_s will maximize V_{oc}, J_{sc} and *FF* and thus power conversion efficiency η.

3.3. Implications for CQD Solar Cell Optimization

The above discussions lead to some useful broad guidelines for CQD solar cell optimization:

(1) Since efficient carrier extraction mandates all photogenerated carriers transit to the electrodes within their lifetime, a simple planar device will require l_{drift} for each carrier that exceeds the depletion region width, and $l_{diffusion}$ greater than the quasi-neutral-region thickness.
(2) Since V_{oc} is determined by the quasi-Fermi level difference across the junction, high doping levels are generally desired (Equation 4). However, high doping density results in thinning of the depletion region (Equation 2), which in turn requires charge carriers to diffuse greater distances through quasi-neutral regions.
(3) Since typical carrier lifetimes in CQD films are on the order of microseconds in the best cases,[24] and since minority carriers need to be extracted over distances on the order of hundreds of nanometers, mobilities of 0.01 cm^2/Vs and well above are desired.
(4) The preceding choice of bimolecular lifetime assumes that radiative recombination limits carrier lifetime; the inclusion of mid-gap states, even at very low density, can dramatically lower lifetimes into the nanosecond regime and below. Excellent passivation of nanoparticle surfaces, eliminating the defect states that lead to mid-gap centers, is thus urgently required.
(5) More limited mobilities may be tolerated, yet complete absorption is achieved, when architectures inspired by organics' bulk heterojunctions[25] and dye-sensitized solar cells' nanoporous electrodes[26] are employed. Majority carrier mobilities in the donor and acceptor phases must nonetheless be maximized (ideally 0.01 cm^2/Vs and above) to minimize the series resistance term in the fill factor.
(6) Strategies to increase absorption per unit length, such as in the case of plasmonics where metal nanoparticles are employed,[27] are also of considerable interest for the same reason.

4. Electrical Properties of CQD Films

4.1. Measurements of Electrical Properties of CQD Film

As discussed in Section 3, carrier mobilities, doping density and carrier lifetime as well as dielectric constant are crucial to modeling photovoltaic device operation. In this section we briefly review the experimental tools that are frequently applied in the field to obtain such physical parameters.

Time of flight (TOF) is used to measure the drift mobility of electrons and holes. It involves photogeneration of a packet of charge carriers via illumination of a semiconductor sample of interest addressed with rectifying electrical contacts.[28] Under an external bias, the photogenerated carriers drift to the collection electrode, leading to the time-dependent current that is monitored across an external load resistor. The choice of bias polarity determines which carrier mobility is measured. Illumination at a short wavelength that ensures substantial absorption of light within a small fraction of the sample thickness ensures that the dimension of the initially-created carrier packet is small compared to the sample thickness in which drift is then observed.

Carrier mobility can be calculated from the transit time t_T, film thickness d and the external bias V:

$$\mu = \frac{d^2}{t_T V} \tag{11}$$

The transit time t_T can be extracted from the intersection point of the asympotes to the double-logarithmic current plotted against time (**Figure 4A**). The absence of a constant-current plateau after the initial current spike indicates dispersive transport.

Successful application of TOF for mobility measurement necessitates that the dielectric relaxation time t_σ exceed the transit time (t_T) of photogenerated carriers:

$$t_\sigma = \frac{\varepsilon_m \varepsilon_0}{\sigma} > t_T = \frac{d^2}{\mu V} \tag{12}$$

where σ is the conductivity. If $t_\sigma < t_T$, the drifting packet of photogenerated carrier will be incapable of reaching the collecting electrode.[29] In addition, TOF measurement also requires t_σ to be longer than the delay time between the application of voltage and the light pulse (t_D).

Carrier extraction by linearly increasing voltage (CELIV) – a purely electronic technique by contrast – follows the transient current induced by the change in the width of the depletion layer in response to a pulsed electrical bias.[29] CELIV enables extraction of the majority carrier mobility. It relies on devices having strong rectification. The linearly increasing voltage is applied through a function generator and the transient current is monitored through a load resistor. Figure 4B shows a representative CELIV transient, from which the hole mobility μ_h may be extracted:

$$\mu_h = \frac{2d^2}{3At_{max}^2(1 + 0.36\frac{\Delta j}{j_d})} \tag{13}$$

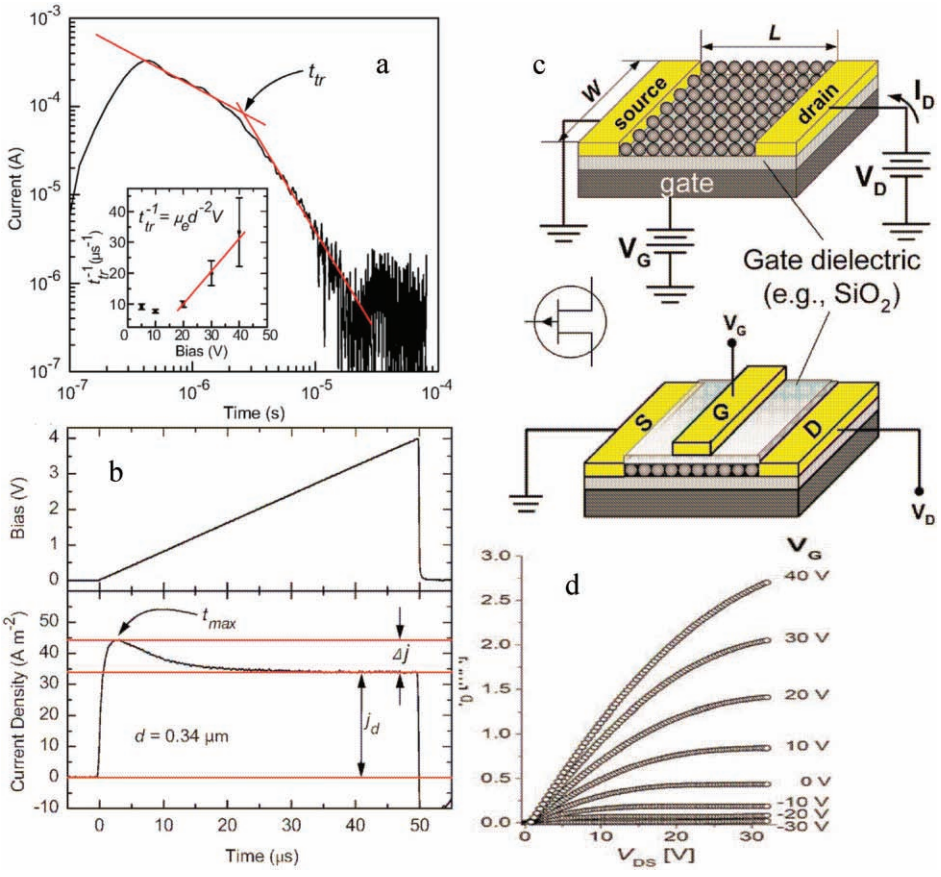

Figure 4. Characterization of carrier mobility. (A) TOF and (B) CELIV measurements of ITO/PbS/Al device. Reproduced with permission.[24] Copyright 2008 American Institute of Physics. (C) schematic diagram of FET configuration (reprinted with permission.[30] Copyright 2010, American Chemical Society) and (D) I_D–V_{DS} plot under different V_G. Reproduced with permission.[31] Copyright 2005, American Association for the Advancement of Science.

d is device thickness, A is ramp rate, t_{max} is the time for the transient current signal to reach its maximum value, ΔJ is the maximum drift current and J_d is the displacement current. CELIV also allows determination of the dielectric constant ε_m of the film:

$$\varepsilon_m = \frac{J_d d}{A\varepsilon_0} \tag{14}$$

The construction and characterization of field-effect transistors (FETs) enables the determination of carrier type and carrier mobility within a semiconductor that serves as channel of the FET.[30] The gate electrode is isolated electrically from source and drain through the use of a thin oxide, typically thermally-grown SiO_2 atop a heavily-doped silicon substrate. Drain and source electrodes desirably form low-resistance contacts to the CQD film. The free carrier density available in the channel, and thus the current flowing between the source and drain upon application of a source-drain bias, is modulated by the gate voltage. For a n-type film, a negative gate voltage depletes the transistor channel, increasing its resistance; while a positive gate voltage enhances the density of free carriers, decreasing its resistance (Figure 4D). The linear regime field effect mobility μ_{lin} of the film can be extracted from the linear regime of drain-source I_D vs gate voltage V_G plot:[31]

$$\mu_{lin} = \frac{L(\frac{\partial I_D}{\partial V_G})}{WC_i V_D} \tag{15}$$

where L is channel length, W is channel width, V_D is drain-source voltage and C_i is the unit capacitance of the dielectric layer:

$$C_i = \varepsilon_m \varepsilon_0 / d \tag{16}$$

ε_m is the dielectric constant (3.9 for SiO_2) and d is the thickness of the dielectric layer.

Another mobility from FET measurement, μ_{sat}, the saturation regime field-effect mobility, can be calculated from the $[I_D]^{1/2}$ versus V_G plot:

$$\mu_{sat} = \frac{2L(\frac{\partial I_D^{1/2}}{\partial V_G})^2}{WC_i} \tag{17}$$

The measured μ_{sat} is usually higher than μ_{lin}, often because the trapping of charge carriers degrades the linear mobility, but these traps are filled by the time the saturation regime is entered. Knowledge of the mobility and measured conductance can then be used to estimate the free carrier density.

The activated doping density of a semiconductor film can also be ascertained from Mott-Schottky capacitance-voltage (C–V) analysis.[32] The doping density can be calculated from the C^{-2} vs V plot:

$$N = \frac{2}{A^2 q \varepsilon_m \varepsilon_0 \frac{dC^{-2}}{dV}} \tag{18}$$

where A is device area and C is the measured capacitance. **Figure 5a** shows a linear fit of C^{-2} vs. V whose slope allows determination of the doping density. When the device is fully depleted, the capacitance is constant during the voltage scan, and dielectric constant ε_m can be obtained from this measurement.

The carrier lifetime may be determined in operating photovoltaic diodes from measurement of the open-circuit decay characteristic.[24,33] Devices are illuminated with a transient pulse that establishes the initial open circuit voltage V_{oc}. Once illumination is turned off, V_{oc} decays at a rate used to estimate the carrier lifetime τ:

$$\tau = -\frac{\kappa T}{q}\frac{F_I}{\frac{dV_{oc}}{dt}} \tag{19}$$

κ is the Boltzmann constant, F_I is a factor ranging 1 at low injection and 2 at high injection, and dV_{oc}/dt is the measured initial slope of V_{oc} degradation. Study of the intensity-dependence of open-circuit voltage decay allows the recombination behaviour of a semiconductor device below and above 1 sun to be explored in detail.

4.2. Transport in CQD Film

As argued above, improved charge transport in CQD films, ideally reaching well above 0.01 $cm^2 V^{-1} s^{-1}$, is prized in realizing high-performance CQD photovoltaics. Transport mechanisms

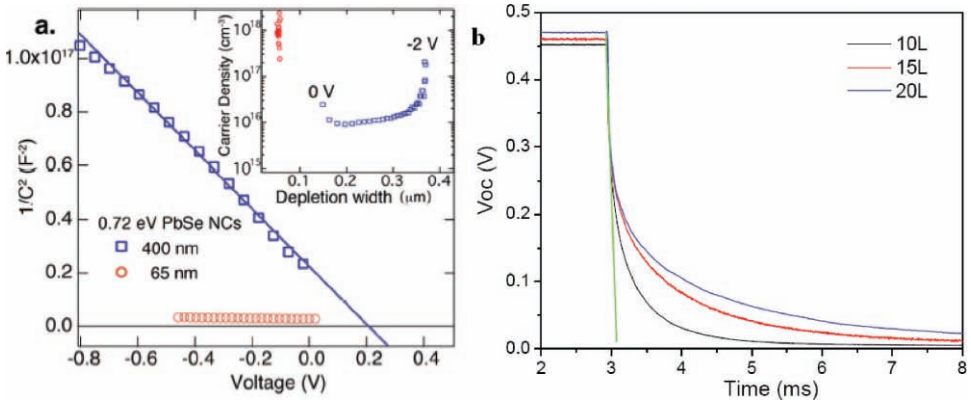

Figure 5. Measurement of doping density and carrier lifetime: (A) C–V analysis of a ITO/PbSe/Al device. Reproduced with permission.[45] Copyright 2008, American Chemical Society. (B) V_{oc} decay analysis of a ITO/PbS/LiF/Al device. The green line is the linear fitting of voltage decay. Reproduced with permission.[33] Copyright 2010, American Chemical Society.

explored include resonant energy transfer,[34] variable range hopping (VRH) and tunneling between adjacent CQDs. We summarize briefly the fundamentals of variable range hopping and tunneling mechanism with emphasis on recent experimental results.

Mott variable range hopping (Mott-VRH) describes low-temperature conduction in strongly disordered systems with localized states.[35,36] Charges localized to having energy E_i may acquire sufficient energy to hop thermally to a nearby site where the energy difference is $\Delta E_{ij} = E_j - E_i$. The spatial distance r_{ij} and energy difference ΔE_{ij} together determine the hopping probability: small r_{ij} and large ΔE_{ij} facilitate the hopping. As shown in **Figure 6A**, when the hopping between nearest-neighbor sites (path I) dominates, the dependence of conductivity on temperature is given by:

$$\sigma = \sigma_0 \exp[-(T_0)\,T)^1] \tag{20}$$

When hopping not between nearest neighbors (path II) also makes a large contribution to the conductivity, the dependence of conductivity on temperature is:

$$\sigma = \sigma_0 \exp[-(T_0)\,T)^{\frac{1}{4}}] \tag{21}$$

where $T_0 = e^2/\varepsilon\alpha$, α is the localization length, and ε is the dielectric constant of the material.

In Efros-Shklovskii variable range hopping (ES-VRH),[37,38] the quantum localization length is assumed to be much smaller than the spatial distance between centers and the overlap between the wave functions is neglected. In this case the relationship between temperature and conductivity is given by:

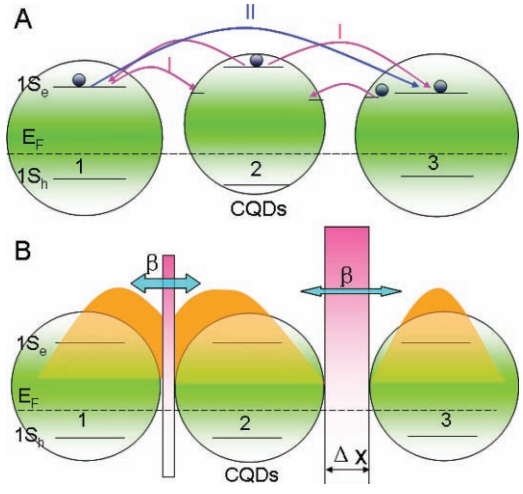

Figure 6. Charge transport in CQD films. Fermi level (dash lines) and the lowest CQD states ($1S_h$ for holes and $1S_e$ for electrons) are depicted. (A) Nearest-neighbor hopping (I) and variable range hopping (I+II) occur between CQD states and surface trap states. Variations in CQD size distribution can produce an energy misalignment between the states among which transport is desired. (B) Tunneling between adjacent CQD allows charge carriers to cross the inter-particle barrier (pink rectangular bar) of width Δx. Exciton delocalization (light orange cloud) and coupling energy β are stronger between CQD 1 and 2 (narrower barrier) than between CQD 2 and 3. While not depicted here, similar pathways for carrier hopping and tunneling also occur within the valance band.

$$\sigma \propto \exp[-(T_0)\,T)^{\frac{1}{2}}] \tag{22}$$

The conduction mechanism change from ES- to Mott-VRH when the energy difference of hopping sites (ΔE_{ij}) equals to the Coulomb gap Δ.[39] In an array of weakly coupled CQDs, the Coulomb gap is:

$$\Delta \approx 2E_c \tag{23}$$

where E_c is the energy required to add or remove one charge to the particle.[30] For a spherical CQD it can be approximately calculated as:

$$E_c = \frac{e^2}{4\pi\varepsilon r} \tag{24}$$

where r is the radius of the CQD.

These concepts have been applied in the study of transport in films consisting of ~5.5 nm diameter PbSe CQDs capped with oleic acid.[40] When the as-produced film was annealed at 373 K, Coulomb blockade dominated because the ~36 meV charging energy E_c for the PbSe CQDs exceeded kT, thus rendering the PbSe CQD film essentially insulating. Annealing at 473 K and higher temperature decreased inter-particle spacing and made the film much more conductive through variable range hopping. Fitting the conductivity as a function of temperature (T) through the following equation (G_0 and T_0 are constants):

$$G = G_0 \exp[-(T_0/T)^p] \tag{25}$$

led to p ~0.95–1.05 in the high-temperature region and ~0.48–0.55 in the low-temperature region, as shown in **Figure 7**. These values closely approach the unity value characteristic of. Mott-VRH and the ~0.5 value characteristic of ES-VRH.[40]

While transport based on hopping is temperature-dependent, transport based on tunneling is temperature-independent. For a general model, the quantum mechanical coupling between two adjacent CQDs can be expressed in terms of coupling energy β:

$$\beta \approx h\Gamma \tag{26}$$

h is Planck's constant and Γ is the tunneling rate, which can be approximated as:[30]

$$\Gamma \approx \exp\left(-2\pi\Delta x\sqrt{\frac{8m^*\Delta E}{h^2}}\right) \tag{27}$$

where m^* is the carrier effective mass and ΔE and Δx are the height and width of the tunneling barrier. The tunneling rate Γ, and also the coupling energy β, drop exponentially with increasing inter-particle distance Δx. The dependence on the barrier height ΔE and carrier effective mass m^* is weaker.[30] As shown in Figure 6B, a larger barrier between CQD 2 and 3 leads to less wave function overlap compared to the wave function overlap between CQD 1 and 2. As in the case of hopping, efficient electron transport requires a coupling energy β that exceeds the Coulomb gap Δ.

The strong dependence of carrier mobility on inter-particle spacing Δx was recently confirmed experimentally by Law et al.[41] PbSe CQD films treated with a series of alkanedithiols were found to exhibit carrier mobilities that decreased

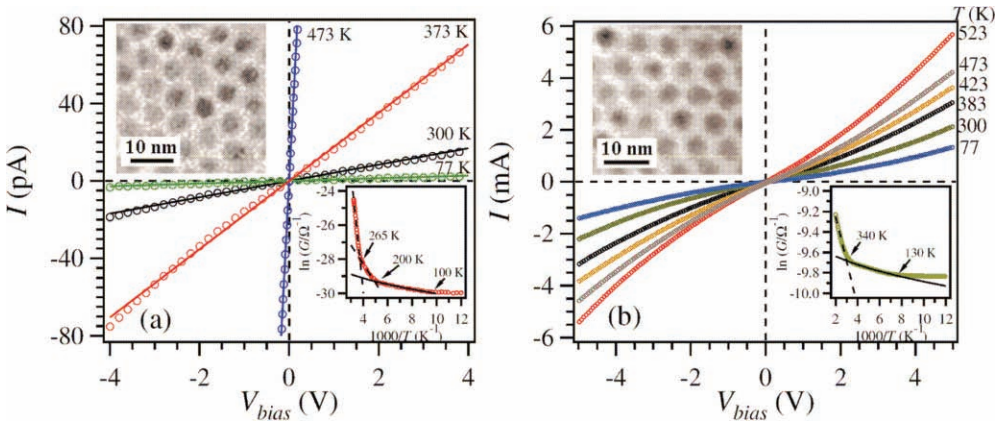

Figure 7. I–V_{bias} characteristics versus T for PbSe CQD film vacuum annealed at (a) 473 and (b) 523 K. The lower insets show G (in log scale) versus the inverse of T. The upper insets are TEM images of PbSe CQDs arrays after vacuum annealing. Reproduced with permission.[40] Copyright 2005 American Physical Society.

exponentially with increasing ligand length. The focus on shrinking the length of organic ligands used in CQD passivation is thus justified.

Exchanging long original ligands to a shorter ligand before film formation is one practice used to decrease inter-particle distance r_{ij}.[42] Following the ligand exchange, smooth and dense film can be directly fabricated using spin-coating or spray deposition. In one study, solution-phase butylamine ligand exchange was used to remove long oleate ligands capping PbS CQDs.[24,43] In a similar vein, molecular metal chalcogenides have recently been employed in solution ligand exchange, producing close packing among $Sn_2S_6^{4-}$-capped CdSe CQDs and $\mu_e \sim 3 \times 10^{-2}$ cm^2 V^{-1}s^{-1}.[44]

Another way to reduce inter-particle distance is to treat the CQD films in the solid phase using short, often bidentate, ligands that substitute the original long ligands. Ligands of interest include methylamine,[45] hydrazine,[31] pyridine,[46] and dithiols such as EDT[47,48] and benzenedithiol (BDT).[49] The deposition of multiple layers is often used to infill cracks resulting from volume contraction. This layer-by-layer strategy has been applied to build films from 8-nm PbSe CQDs treated using 1.0 M hydrazine. Impressive $\mu_e \sim 0.7$ cm^2 V^{-1} s^{-1} for as-treated films and μ_h of 0.12–0.18 cm^2 V^{-1} s^{-1} for films exposed to air were obtained.[31] Similar solid-state treatments of PbSe CQD film using alternative ligands and linkers have been reported.[50,51]

Methods that combine solution-phase and solid-state treatments may be beneficial. In one report, PbSe CQDs were first exchanged from oleate to octylamine in solution, after which films were fabricated using layer-by-layer processing. These films were further treated with BDT and $\mu_e \sim 1.4 \times 10^{-3}$ cm^2 V^{-1} s^{-1} and $\mu_h \sim 2.4 \times 10^{-3}$ cm^2 V^{-1} s^{-1} were obtained.[49] A similar strategy was applied in the case of PbS CQD films.[23] The use of BDT was advanced as a means to promote electron delocalization by virtue of the conjugated benzene ring, a means to decreasing barrier height ΔE and increasing coupling energy β.

Table 1 summarizes the electron and hole mobilities reported for different CQD films. The range of reported mobility values is expected to arise due to differences in inter-particle spacing resulting from the various treatments. As seen in Equation 27, a small variation in Δx may lead to a large change in the coupling energy and measured mobility. Different methods of mobility characterization are also expected to produce discrepancies in reported mobilities. In FET mobility measurements, the applied gate bias will result in filling of the deeper traps, and the modulation of the current flowing through the channel will reveal the

Table 1. Reported electron and hole mobilities for various CQD films.

Material	Film Preparation	Ligand	CQDs size	μ_e (cm^2 V^{-1} s^{-1})	Measurement technique	μ_h (cm^2 V^{-1} s^{-1})	Measurement technique	ref.
PbS	solution exchange	butylamine	6 nm	$(2 \pm 1) \times 10^{-4}$	TOF	$(1.5 \pm 0.1) \times 10^{-3}$	CELIV	[24]
CdSe		$Sn_2S_6^{4-}$ + heat treatment	4.5 nm	3×10^{-2}	FET			[44]
PbSe	solid state treatment	hydrazine	8 nm	0.7	FET	0.12–0.18	FET	[31]
		hydrazine	7.4 nm	0.5–1.2	FET			[50]
		EDT	6.1 nm	0.07	FET	0.028	FET	[41]
PbS	mixed[a]	butylamine + 1,4-BDT	6 nm	$(1–6) \times 10^{-4}$	transient photocurrent			[23]
PbSe	mixed	octylamine + 1,4-BDT	4 nm	1.4×10^{-3}	FET	2.4×10^{-3}	CELIV	[49]

[a] the third strategy: first solvent exchange then solid-state treatment.

high mobilities associated with shallow traps and subbands.[19] In CELIV and TOF measurements, traps are more prone to dominate mobility measurements, leading to smaller extracted mobility values.

It should be emphasized that quantum confinement in CQDs should be substantially preserved in order to maintain high V_{oc}. Hence, it is important to monitor the preservation of an excitonic peak in absorption[48] and/or quantum efficiency spectra in films and devices following ligand exchanges and film fabrication.

4.3. CQD Passivation

As discussed in Section 3.1, midgap defects in devices act as recombination centers. They reduce the number of extractable photogenerated carriers, leading to suboptimal internal quantum efficiency and thus J_{sc}. They also suppress quasi-Fermi level splitting under illumination, decreasing the available V_{oc}. Passivation of these midgap defects is therefore crucial to achieve efficient solar cells. In solution-based studies of CQD luminescence, there is no limit on the ligand length that can be used to enhance passivation;[52,53] however, in optoelectronic applications such as photovoltaics, good carrier transport mandates a small inter-particle spacing requiring the use of short – yet still strongly passivating – ligands.

Recent findings have established lead chalcogenide CQDs as composed of a stoichiometric core surrounded by a Pb-rich cation layer.[20,21] This nonstoichiometric nature has been found to simplify the implementation of complete passivation. Ligands that bind strongly only to surface cations may substantially passivate surface defects. Pb-rich nanoparticles passivated using short thiols – ligands that are minimal in volume and high in affinity to surface Pb^{2+} – have therefore seen considerable attention.

The nature of the defects – whether they produce deep midgap recombination centers or more innocuous shallow traps – depends on chemical treatment. Related work on the temporal response of PbS CQD photoconductive photodetectors showed that both amine and carboxylic acid-terminate ligand treatments resulted in long-lived defects having > 2 second time constants. These long-lived – hence energetically deep – traps were associated chemically with the presence of $PbSO_4$ on the surface of the nanoparticles. Once treated with thiol-terminated ligands, these films exhibited only the presence of $PbSO_3$ and evinced a much shorter-timescale temporal response consistent with shallow traps.[54]

The choice of ligand end functional group has a correspondingly dramatic influence on photovoltaic device performance. Vapor treatment using ethanethiol improved PbS CQD photovoltaic device performance.[55] Following the passivation of midgap recombination centers on the PbS CQD surface, V_{oc} increased from 0.28 to 0.43 V and EQE increased from 5% to 22%, leading to a 10-fold improvement in device efficiency. Another study revealed that EDT treatment not only removed all oleate ligands from PbSe CQDs, but also effectively passivated the CQDs and produced photovoltaic devices having internal quantum efficiency of greater than 80%.[48]

Whereas short-thiol-based ligands have shown great success in CQD passivation for photovoltaic devices, they suffer from two major limitations:

1) Due to their small molecular weight, many of these ligands are volatile and may be readily removed under thermal annealing.[56,57] Relatedly, metal-sulfur moieties are susceptible to oxygen attack, leading to devices having poor air stability.
2) Most thiol-based ligands explored to date passivate surface cations, leaving the surface anions incompletely passivated.[58] These unpassivated anions may yield midgap recombination centers and deteriorate device performance.[59]

The epitaxial growth of a thin wide-bandgap semiconductor shell around the CQD core offers one potential solution to overcome these limitations. In the solution phase, this approach has been found to improve the photoluminescence yield of CdSe CQDs by the growth of ZnS shell.[60] Even when the shell is not epitaxial to all facets of the core, such as in the PbS/CdS core/shell system, photoluminescence emission intensity has been seen to improve appreciably.[61,62] Related systems such as PbSe/PbS and PbSe/$PbSe_xS_{1-x}$ core-shell CQDs,[63,64] as well as PbSe/PbS core-shell nanowires,[65] have seen similar study.

To date, only air stability and photoluminescence yield[66,67] – and not absolute device performance – have been reported for lead chalcogenide core/shell CQDs. Shell growth, while reducing surface defects, is expected to come at a cost to carrier transport. Core/shell CQDs generally confine one (type II core-shell) or two (type I core-shell) carrier wave function inside the core, militating against delocalization of either both or one charge carrier. A delicate balance between surface passivation and carrier transport necessitates the careful engineering of ultrathin shell growth.

4.4. CQD Film Doping

Both doping type and doping density are important for the operation of photovoltaic devices. A p-type CQD film is required for Schottky devices that employ shallow work function metals. Doping density is a crucial variable in device operation: increasing doping density (N_A and N_D) will increase contact potential V_0 (Equation 4) but decrease the depletion region thickness W (Equation 2).

Doping CQD films based on the deliberate introduction of specific impurity ions into the core remains a challenge. Self-purification – wherein dopants segregate out from the core to the surface – results because the formation energies of defects increases as the size of the nanocrystal decreases.[68,69] Recent experimental observations by several groups have nonetheless confirmed the doping of CQD film. In one report, a hydrazine-treated PbSe CQD film originally was n-type. After vacuum treatment or mild heating, the film switched to p-type.[31] Similarly, butylamine-capped PbS CQD film has been shown to exhibit p-type behavior based on Mott-Schottky analysis.[24]

Successful doping of CQD film can be explained with reference to the formation of traps at the CQD surface. Unpassivated surface atoms – either cations or anions – can, by trapping free carriers, act equivalently to donors if they trap holes, or to acceptors if they trap electrons. The net doping density is the difference between the number of electron-capture defects and the number of hole-capture defects. Treatments applied to CQD films will naturally influence the number of each type of surface defects and thus change the net doping type and density.

Hole density has been observed to equal to 3×10^{16} cm^{-3} for untreated PbS CQD films and to vary from 2×10^{16} cm^{-3} to 1×10^{17} cm^{-3} following EDT treatment and air annealing, respectively.[47] These findings may be explained by noting that EDT passivates surface defects and thus reduces film doping density; whereas air annealing removes EDT and re-exposes surface defects, leading to an increased doping density.

The density of the quantum dots themselves in CQD films lies in the vicinity of 10^{19} cm^{-3} for the case of ~3 nm dots. For measured N_A of order 10^{17} cm^{-3},[33] this corresponds to only one acceptor per >100 nanocrystals. This is low considering the abundant surface area of the materials, and is suggestive that thiols are indeed highly effective in passivation.

An alternative means of doping CQD film involves combining two types of nanoparticles. A 1:1 composite of PbTe:Ag_2Te nanocrystals was found to exhibit a 100-fold increase in conductivity compared to pure-phase PbTe and Ag_2Te films.[70] Because of the staggered band diagram between PbTe and Ag_2Te nanoparticles, electrons move from Ag_2Te nanoparticles to fill the trap states of neighboring PbTe nanoparticles, leaving mobile holes in Ag_2Te nanoparticles that increase the conductivity of this p-type film.[71] This finding suggests that CQD mixtures may be used to tune the net doping of CQD film.

4.5. Dielectric Constant of CQD Film

The dielectric constant ε_m of CQD films is relevant to the depletion region width (Equation 2). The dielectric constant of CQD films is expected and observed to be lower than that of their bulk counterparts[72] from volume fraction considerations.[33] In Maxwell-Garnett effective medium theory, this can be explained quantitatively as:

$$\varepsilon_m = \varepsilon_1 \frac{\varepsilon_2(1+2\delta) - \varepsilon_1(2\delta - 2)}{\varepsilon_1(2+\delta) + \varepsilon_2(1-\delta)} \quad (28)$$

where ε_1 and ε_2 are the dielectric constant of the matrix and embedded material and δ is the volume fraction of the embedded material. As one example, taking volume fraction δ of 0.5 and ε_2 of 50 for the quantum dot phase, and ε_1 of 4 for the remaining volume occupied by ligands, results in a predicted dielectric constant of 12 for a typical PbSe CQD film. This is in good agreement with capacitance-voltage results that allow extraction of the effective dielectric constant of the film.[45] Both CELIV and C-V measurements also indicate the typical PbS CQD film effective dielectric constants are in the range 15–20.

5. Progress in CQD Solar Cell Performance

Ever since the first observation of photovoltaic effect from PbS CQDs in 2005,[42] rapid progress has been achieved in this field. The AM1.5G efficiency has now reached 5.1%. Various device architectures, including metal/CQD film, oxide/CQD film, organic layer (polymer or small molecules)/CQD film, and CQD film/CQD film, have been explored. The nature of photovoltaic device operation – excitonic solar[73] vs. p-n heterojunction mechanisms[43,45] – remains a lively topic within the published literature.

5.1. Schottky Solar Cells

The junction between a p-type semiconductor and a low work function metal (Al, Ca, Mg etc.); or between an n-type semiconductor and a deep work function metal (Au, Pt, etc.) forms a Schottky contact. Because lead chalcogenide CQD films are generally p-type, the preponderance of published Schottky barrier photovoltaic work employs shallow work function metals. In these devices, band bending occurs only inside the CQD film. A depletion region is established and the resultant internal field separates electron-hole pairs. Electrons flow into the metal, and holes to a transparent deep-work-function ohmic contact such as ITO and FTO.

The first CQD solar cells to exceed 1% AM1.5 PCE were reported in 2008[43] and employed a Schottky architecture. PbS CQDs underwent a solution-phase ligand exchange to replace original oleate ligands (~ 2.5 nm) with much shorter (~0.5 nm) butylamine. Spin-coating of these nanocrystals from octane solution led to smooth, densely packed arrays, as shown in **Figure 8a**. A Schottky barrier was formed at the junction between Al and the PbS CQD film. The device showed an AM1.5G efficiency of 1.8% with a V_{oc} of 0.33 V and a J_{sc} of 12.3 mA/cm^2. The PbS CQD film had μ_h of $(1.5 \pm 0.1) \times 10^{-3}$ cm^2 V^{-1} s^{-1} and μ_e of $(2 \pm 1) \times 10^{-4}$ cm^2 V^{-1} s^{-1}. Drift lengths l_{drift} for holes and electrons in the depletion region were found to be 10 μm and 1 μm, respectively. The diffusion length $l_{diffusion}$ for minority electrons in the quasi-neutral region was estimated to be 0.1 μm. The majority of collected photocarriers were generated and effectively separated in the depletion region, and the efficiency of the device was limited by the rate of carrier diffusion through the quasi-neutral region.[43]

Soon thereafter, a Schottky device was reported that employed PbSe CQDs that were brought together and passivated using treatment with 1,4-benzenedithiol.[49] It is believed that some of these bidentate thiols bind to the surface of the same nanocrystal, while others may bridge nearby particles. These devices showed an AM1.5G efficiency of 1.1% and offered a significant improvement in air stability over the butylamine-based devices.

Later in 2008, a Schottky device using PbSe CQDs and having an AM1.5G efficiency of 2.1% was reported (**Figure 9**).[45] EDT was used to treat the film. It served both to remove the long oleate ligand and to passivate the PbSe CQDs. A layer-by-layer dip-coating strategy was again applied such that any cracks and pinholes from the EDT treatment were filled in using the next layer. An impressive short-circuit current density J_{sc} of 24 mA cm^{-2} was obtained; the low V_{oc} of 0.239 V and *FF* of 40.3% account for the overall efficiency. The EQE spectrum reached 55–65% at wavelengths shorter than 800 nm, photon frequencies for which absorption of light was substantially complete. The ~80% internal quantum efficiency estimated in this part of the spectrum indicates minimal recombination loss and efficient carrier extraction. By building devices having different bandgaps, the authors found that the open-circuit voltage V_{oc} of the device depended on E_g according to $V_{oc} \approx 0.49 (E_g/q) - 0.253$ V. This pinning relative to the half-bandgap of the semiconductor is often seen in Schottky devices.[74] V_{oc} was observed to decrease with increasing work function of the top metal contact, as expected for a Schottky solar cell.

In 2009, the efficiency of CQD Schottky device was improved to 3.3% by employing ternary PbS_xSe_{1-x} CQDs. Devices attained a V_{oc} of 0.45 V and a J_{sc} of 14.8 mA/cm^{-2}. The

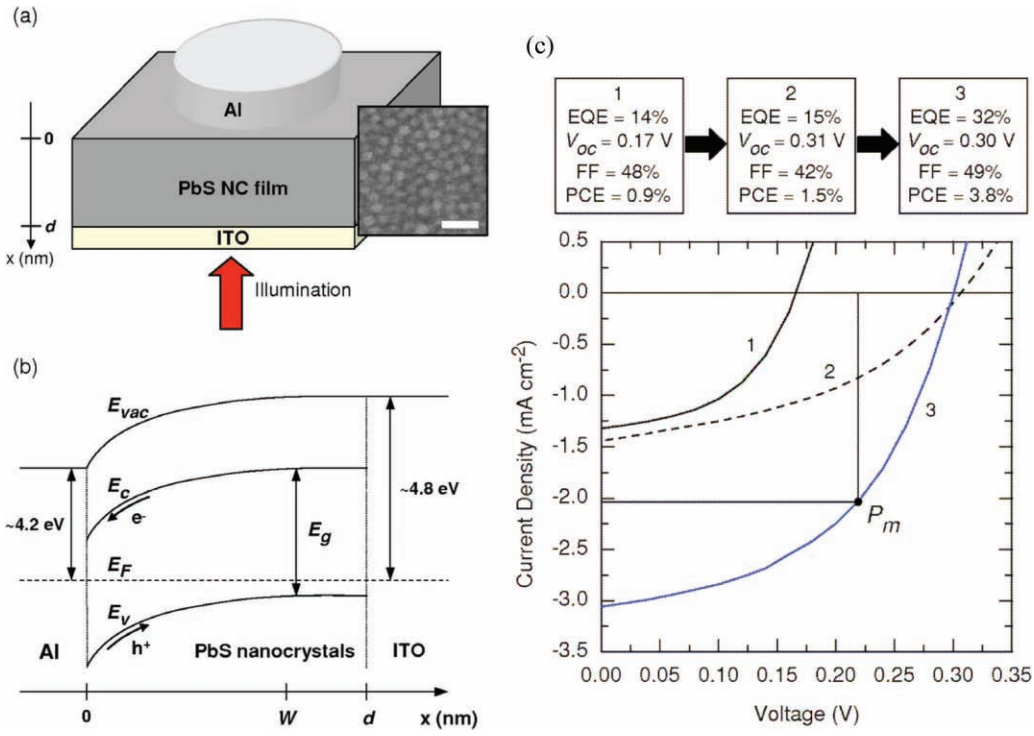

Figure 8. (a) Depiction of the architecture of a typical CQD-Schottky device. The inset shows an SEM image of the nanocrystal film (scale bar is 20 nm). (b) The energy band model. (C) The *J–V* curve and photovoltaic performance (under 975 nm, 12 mW cm^{-2} illumination) for the baseline device (1), device processed using the fast cooling PbS CQDs (2) and device further employed butylamine ligand exchange (3). Reproduced with permission.[43] Copyright 2008 American Physical Society.

authors ascribed the higher efficiency to the synergetic effect of the alloyed PbS_xSe_{1-x} CQDs.[75] In 2010, the efficiency of PbS CQD Schottky device was further improved to 3.6%. Small and conjugated molecules *N*-2,4,6-trimethylphenyl-*N*-methyldithiocarbamate (TMPMDTC) were used as ligands and benzenethiol was applied to treat the film during layer-by-layer coating. LiF/Al was used as the Schottky contact and the devices showed a record V_{oc} of 0.51 V, J_{sc} of 14.0 mA/cm^{2,} and FF of 51%.[76]

While Schottky devices benefit from straightforward fabrication, their efficiency is limited by three factors:

1) Light absorption begins at the transparent conductive oxide side, requiring that the highest density of photogenerated minority electrons travel through much of the film thickness before reaching the electron-collecting Schottky contact. These carriers are vulnerable to loss via recombination.

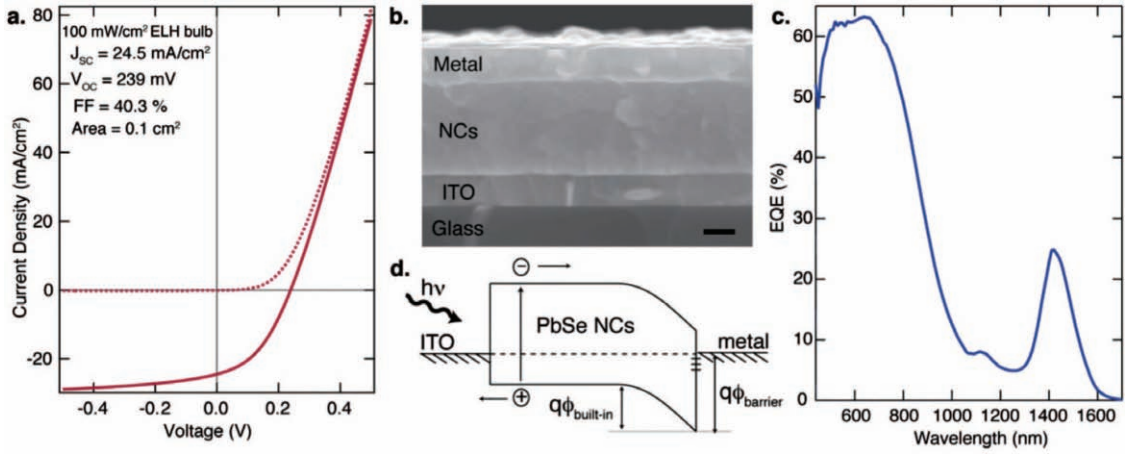

Figure 9. Structure, performance and schematic diagram of the ITO/PbSe/Ca Schottky device. (a) *J–V* characteristics of a representative device in the dark and under simulated AM1.5G illumination. (b) SEM cross-section of the device stack. (c) EQE spectrum of a 140 nm-thick device (PbSe CQDs *Eg* = 0.95 eV). (d) Proposed equilibrium band diagram. Reproduced with permission.[45] Copyright 2008, American Chemical Society.

2) For an ideal Schottky junction, the barrier height is typically limited to ~0.67 E_g, while in practical devices the V_{oc} is often lower because of the Fermi-level pinning by defect states at the metal-semiconductor interface.
3) A minimal barrier to hole injection is present at the electron-extracting electrode of the Schottky device, limiting shunt resistance and inviting back-recombination.

5.2. Heterojunction Solar Cells

Heterojunction solar cells have recently been shown to overcome each of the key limitations of the Schottky architecture.[77] In the highest-efficiency CQD photovoltaics reported to date, a p-n heterojunction was formed by bringing together two semiconductors of opposite doping type and generally different composition and bandgap. For efficient dissociation of photogenerated carriers, the donor and acceptor materials should form a type II heterojunction: the (electron) acceptor – the n-type material – should have a lower conduction band level while the (electron) donor – the p-type material – should attract holes. Quantum size-effect tuning provides an added degree of freedom, beyond material composition alone, in the manipulation of the band position of CQDs. Consequently, the restriction on the material selection for appropriate band offset is significantly relaxed and more materials are available for CQD heterojunction solar cells.

Sensitizing nanocrystal TiO_2 solar cells using InAs CQDs[78] has been found to lead to efficient charge transfer from InAs CQDs to TiO_2 particles without deliberate modification of the quantum dot capping layer. For the InAs CQDs sensitized solar cell using a Co^{2+}/Co^{3+} electrolyte, devices showed ~1.7% efficiency under 5 mW/cm^2 illumination but decreased to 0.3% under 1 sun illumination. HgTe CQDs have also been used to sensitize nanoporous TiO_2 electrodes and extend the photon-harvesting spectral regime to 1500 nm.[79] HgTe CQDs, either aqueous soluble or organic-solvent-soluble, were mixed with nanoporous TiO_2 electrodes and a poly(3-hexylthiophene) (P3HT) matrix to combine the concepts of nanocrystal/polymer-blend solar cells and a solid-state nanocrystal-sensitized solar cell. The devices showed improved J_{sc} compared to a control device without HgTe CQDs, suggesting a role for HgTe CQDs in infrared light absorption.

Polymers and small organic molecules have also been applied to build CQD heterojunction solar cells.[80] Hybrid heterojunction photovoltaic cells using 1,3-BDT crosslinked PbS CQDs and vacuum-deposited C_{60} layer achieved an AM1.5G efficiency of 2.2%, compared to 1.6% in the corresponding Schottky device.[81] The increase in efficiency arose largely from the V_{oc} and *FF* improvement due to the reduced recombination current and higher carrier collection efficiency at the PbS CQDs/C_{60} interface, an intrinsic advantage associated with a well-engineered heterojunction device.

A photovoltaic device based on PbS CQDs and amorphous silicon (a-Si) was reported in 2009.[82] The device showed a V_{oc} of 0.2 eV, a J_{sc} of 4.13 mA cm^{-2}, a *FF* of 0.39, corresponding to an efficiency of 0.9% under 36.5 mW cm^{-2} xenon lamp illumination. EQE reached 50% at ~500 nm in the device and both a-Si and PbS CQDs contributed to the photocurrent. During operation, photogenerated electrons flowed to a-Si and were collected using an Al electrode; and holes flowed from a-Si through PbS CQDs to ITO, corresponding to a p (PbS) – n (a-Si) junction device.

Heterojunction devices based on PbSe CQDs and ZnO film have been reported with an AM1.5G efficiency of 1.6%.[83] As shown in **Figure 10**, the device was composed of a ZnO film made using rf magnetron sputtering; a layer-by-layer dip-coated PbSe CQD film treated using EDT; an

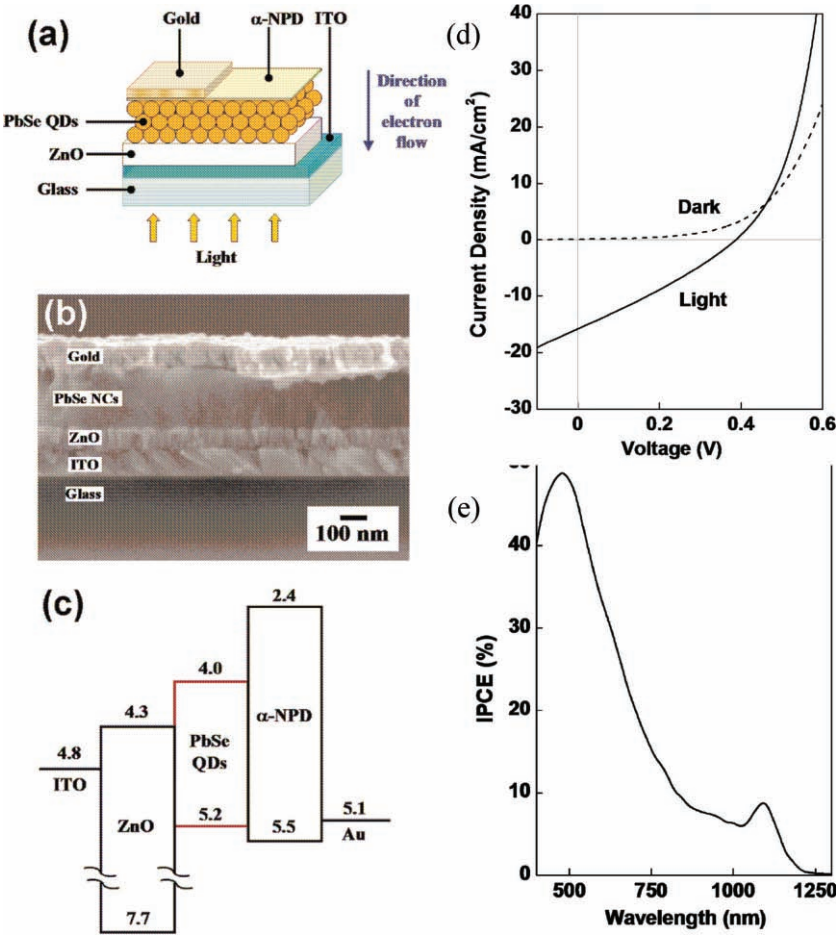

Figure 10. (a) Schematic and (b) cross-sectional SEM image and (c) energy band diagram of the ITO/ZnO/PbSe CQDs/α-NPD/gold heterojunction solar cell. (d) *I–V* characteristics of the cell recorded in the dark and under simulated AM1.5G illumination and (e) its corresponding EQE spectrum. Reproduced with permission.[83] Copyright 2009 American Chemical Society.

electron-blocking layer α-NPD [*N, N*′-bis(1-naphthalenyl)-*N, N*′-bis(1-phenylbenzidine)]; and an ohmic gold contact deposited via thermal evaporation. Electrons were injected from the PbSe layer into to the ZnO as seen in Figure 10c. The device showed a J_{sc} of 15.7 mA cm^{-2} under simulated AM1.5G illumination. The optimal thickness for the PbSe film was determined to be ~100 nm, a balance between absorption and carrier transport; and the optimal thickness for α-NPD layer was determined to be ~30 nm, a balance between shunt resistance gain (improved V_{oc}) and series resistance loss (decreased J_{sc}).

The record-setting CQD solar cells recently reported reached above 5% AM1.5 solar power conversion efficiencies for the first time (**Figure 11**).[77] These devices – known as depleted-heterojunction colloidal quantum dot solar cells (DH-CQD) – took advantage of an heterojunction between a transparent n-type TiO_2 electrode and an active layer consisting of PbS CQDs. The 1S electron excited state of the CQD lies well above (>0.3 eV) the TiO_2 conduction band level: photoexcited electron injection was favored therefore into TiO_2 both due to the band offset and the built-in potential from the p-n diode junction. The 1P hole level exhibits a large (> 1.5 eV) discontinuity with the TiO_2

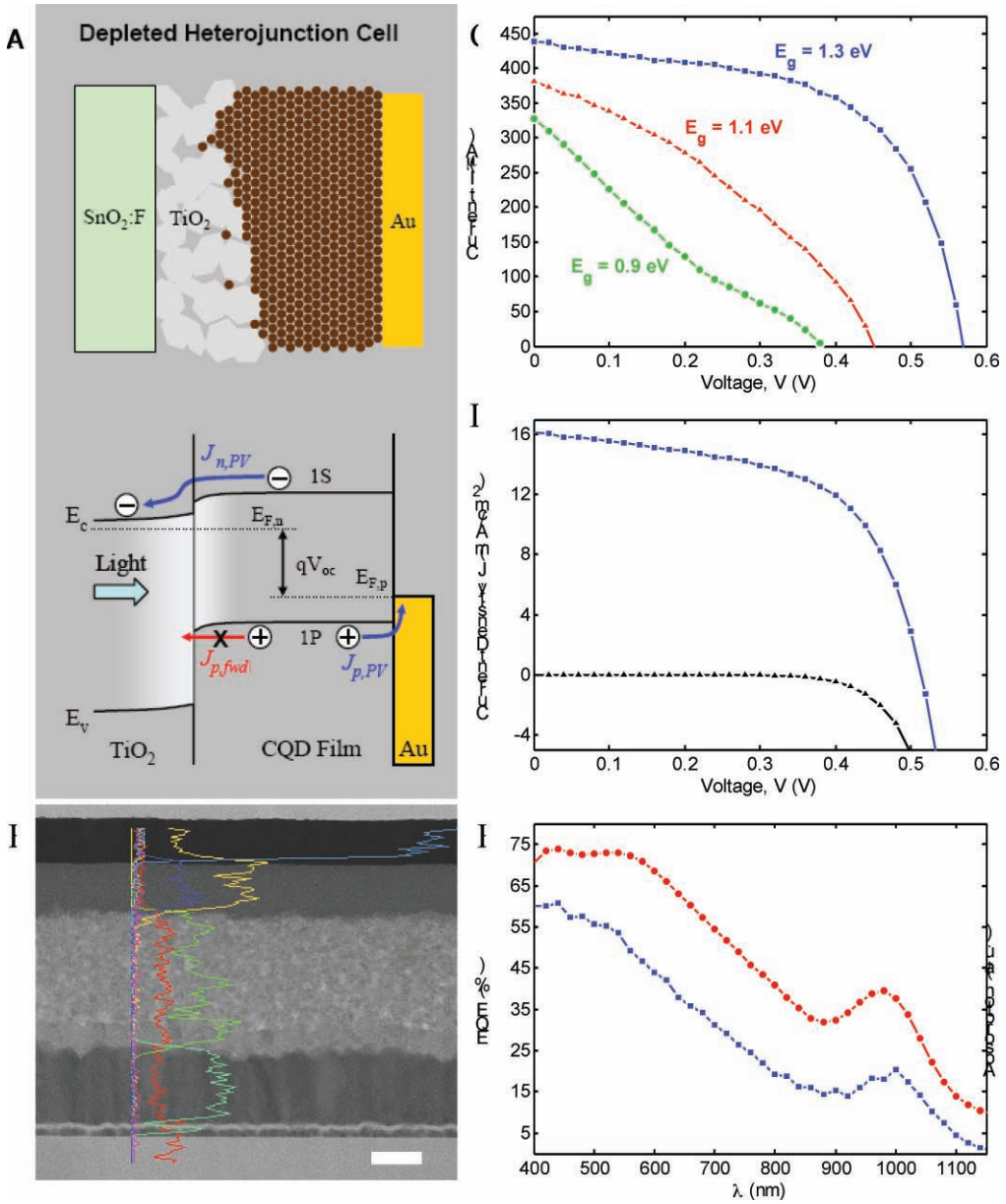

Figure 11. Device architecture and performance of TiO_2/PbS heterojunction solar cells. (A) Schematic demonstration of FTO/TiO_2/PbS/Au and its band diagram; (B) Cross-sectional TEM as well as elemental distribution plot of a photovoltaic device. The scale bar is 200 nm; (C) *I-V* response of devices using three different size CQDs; (D) *J–V* curves for the champion device recorded with and without one sun illumination; (E) EQE and absorption spectra of the champion device. Reproduced with permission.[77] Copyright 2010 American chemical Society.

valence band, providing a sizeable barrier against the undesired passage of majority holes from the p-type CQD layer into the TiO_2 electrode. Holes were conducted away using a top ohmic Au contact to the p-type PbS CQD layer.

DH-CQD photovoltaics successfully overcame the limitations of prior work on Schottky barrier CQD devices in three principal ways. First, the DH design employed a transparent electron-accepting TiO_2 contact, thereby benefiting more efficiently from minority carrier separation due to the placement of the junction on the illuminated side. Second, whereas the Schottky device's open-circuit voltage is limited by Fermi-level pinning due to defect states at the metal-semiconductor interface, the TiO_2-CQD interface benefited from passivation during the solution-phase deposition of the quantum dots. Third, a large discontinuity in the valence band of the DH device, combined with the minimization of electron density in the electron acceptor near the junction, maximized shunt resistance to enhance fill factor and minimized back-recombination to improve V_{OC}.

Under 0.94 sun illumination, the best devices showed a V_{oc} of 0.51 V, a J_{sc} of 16.2 mA cm^{-2}, and *FF* of 58%, corresponding to an efficiency of 5.1%. The improvement in performance over previous reports derives principally from improved V_{oc} and *FF*, both traceable to the improved device architecture. The shape of the EQE spectrum resembled its absorption spectrum and reached a maximum value of 60%.

For the PbS CQDs used in these devices, simple calculation suggests that Förster energy transfer should allowed the transport of excitons over distances corresponding to at most a few quantum dots dots; however, efficient carrier extraction occurred in this 200–250 nm thick PbS CQD film. Additionally, the V_{oc} in devices made using CQDs having different size-tuned bandgaps was found to correlate closely with the Fermi level difference. These observations lend additional support to the p-n junction picture of device operation presented herein.

In all CQD devices reported to date, the EQE spectrum has yet to approach its potential. High-efficiency solar cells having an EQE exceeding 90% above the bandedge would lead to J_{sc} > 35 mA/cm^{-2}. Efforts to minimize recombination loss and maximize film absorption are thus of great importance to improve device efficiency.

We summarize recent reports on photovoltaic device performance from various infrared CQDs in **Table 2**.

6. Device Stability

Solar cells based on infrared CQDs had initially been reported to suffer from poor stability. Stored in air, butylamine-capped PbS CQD devices degraded within minutes.[43] Significant progress was made when 1, 4-BDT treated PbSe CQD devices were found to be stable in a glove box over weeks and in air over a few hours.[49] In contrast, EDT-treated PbSe devices lost performance completely even within a few minutes' air exposure.[45,82]

The mechanisms underlying device degradation have recently been investigated systematically.[84] Two key and independent

Table 2. Summary of device performance based on infrared CQDs.

CQDs material	Device architecture	V_{oc} (V)	J_{sc} (mA cm^{-2})	FF	AM1.5G efficiency	reference
PbS	Au/P3HT/PbS/ITO [a]	0.4	0.13	0.38	0.02%	[86]
	ITO/SnS/PbS/Al	0.35	7.22	0.32	0.37	[87]
	ITO/PbS/a-Si/Al	0.2	8.99	0.39	0.7%	[82]
	ITO/PbS/Al	0.33	12.3	0.44	1.8%	[43]
	ITO/PbS/LiF/Al	0.46	8.57	0.545	2.15%	[33]
	ITO/PbS/C60/LiF/Al	0.40	10.5	0.52	2.2%	[81]
	ITO/PbS/LiF/Al	0.51	14.0	0.51	3.6%	[76]
	FTO/TiO_2/PbS/Au	0.51	16.2	0.58	5.1%	[77]
PbSe	ITO/PEDOT/(BP:PbSe)/PbSe/Al [b]	0.65	0.0258	0.22	0.003%	[88]
	ITO/PEDOT/P3HT/P3HT:PbSe/Al	0.41	1.01	0.46	0.19%	[89]
	ITO/MOPphotovoltaic-MWNT:PCBM/PbSe/Al [c]	0.406	1.71	0.35	0.40%	[90]
	ITO/PbSe/Al	0.24	12	0.38	1.1%	[49]
	ITO/PbSe/PEDOT:PSS/P3HT:PCBM/Al [d]	0.57	6.38	0.32	1.17%	[91]
	ITO/ZnO/PbSe/α-NPD/Au [e]	0.39	15.7	0.27	1.6%	[83]
	ITO/PbS_xSe_{1-x}/Al	0.45	14.8	0.50	3.3%	[75]
	ITO/PEDOT:PSS/PbSe/ZnO/Al	0.44	24	0.32	3.4%	[75]
InAs	FTO/TiO_2/InAs/electrolyte/Pt	0.35	1.8	0.48	0.3%	[78]
HgTe	ITO/TiO_2/(HgTe:TiO_2)/(HgTe:P3HT)/Au	0.40	2	0.5	0.4%	[79]

Note: [a] P3HT: poly(3-hexylthiophene); [b] PEDOT: poly(3,4-ethylenedioxythiophene), BP: tetrabenzoporphyrin; [c] MOPphotovoltaic-MWNT: poly[(2-methoxy, 5-octoxy)-1,4-phenylenevinylene]-multiwalled carbon nanotubes; [d] PSS : poly(styrene-sulfonate), PCBM phenyl-C61-butyric acid methyl ester; [d] α-NPD [N,N′-bis(1-naphthalenyl)-N,N′-bis(phenylbenzidine)].

mechanisms have now been pinpointed. First, degradation of the metal-semiconductor interface has been identified and successfully addressed. Second, the loss of passivation within the film, leading to the development of midgap recombination centers, has also been identified and remedied.

Ultimately these new insights have enabled processing of devices entirely within an air ambient instead of requiring glovebox processing. The best stability results reported >60 hours of continuous and simultaneous 100 mW cm^{-2} AM1.5G illumination and current-voltage scanning in an air ambient. The unencapsulated devices retained ~87% of their initial power conversion efficiency, as shown in **Figure 12**. These devices exhibited an AM1.5G efficiency of 2.1%. This dramatic improvement in device stability originated from two factors:

1) The distinctive surface-chemical properties of small PbS CQDs (~3 nm). Small PbS CQDs have been reported to be more spherical than larger particles, and also have a higher Pb:S ratio compared with the more faceted large PbS CQDs. Ligands binding to surface lead cations form a dense ligand shell, blocking oxygen access and protecting CQD films from oxidation. In contrast, large PbS CQDs include exposed {111} facets consisting of sulfur anions not protected by thiol-terminated ligands. Oxygen can easily attack these unprotected {111} surfaces (as shown in Figure 12D). XPS studies reveal that the main oxidation product of small PbS CQDs is $PbSO_3$, a shallow trap state with a trap depth of 0.1 eV.[54,85] In contrast, the main oxidation product of large PbS CQDs is $PbSO_4$, a deeper midgap state. Thus, oxidation of small PbS CQDs is impeded, and the oxidation products are more inoccuous shallow traps; oxidation of large PbS CQDs occurs more readily and the oxidation products are recombination centers. These findings account for the improved air stability of the PbS CQD films themselves.[33]
2) A Schottky contact engineered for air stability. Initial Schottky devices had employed Al metal in direct contact with CQD films. Subsequent control experiments revealed that using an Ag electrode instead led to enhanced air stability, though inferior absolute initial performance. These initial findings suggested that a component of photovoltaic device degradation was occurring at the metal-semiconductor interface. Sandwiching a very thin (nominally 0.8 nm) LiF between the Al electrode and the CQD film suppressed the interfacial reaction and dramatically improved air stability. The LiF:Al electrode also benefited from improved open-circuit voltage, leading to the device with improved overall AM1.5 power conversion efficiency.[84]

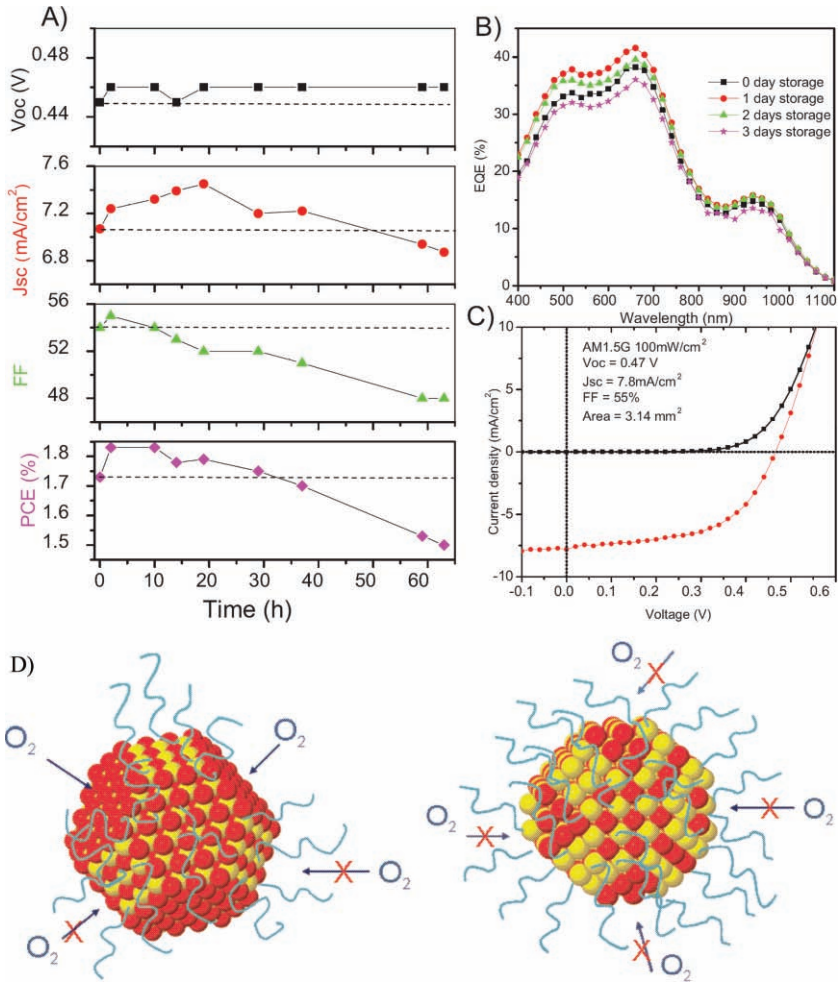

Figure 12. Device performance, stability and its origin of PbS CQD Schottky device. (A) Device performance tracking (V_{oc}, J_{sc}, *FF*, and AM1.5G PCE) measured in air under simultaneous and continuous *I–V* scanning (linear scan from –1 V to 1 V, 100 ms per 0.02 V) and simulated AM1.5G irradiation; (B) Temporal evolution of EQE spectra of devices stored in an air ambient; (C) Representative device performance in the dark and under AM1.5G irradiation. (D) Schematic illustration of oxidation for large (left) and small (right) PbS CQDs. Large PbS CQDs are faceted and small ones are spherical. The red spheres, yellow spheres, and cyan tails are dedicated to sulfur atoms, lead atoms in PbS CQDs, and surface ligands, respectively. Panels A, B, C are reprinted with permission.[84] panel D is reprinted with permission.[33] Copyright 2010, American Chemical Society.

7. Perspectives and Conclusions

Infrared CQDs are promising functional materials that hold great potential for low-cost and/or high efficiency solar cells. Since the first report of a photovoltaic effect from PbS CQDs in 2005, rapid progress has been achieved in the past 5 years, with the latest AM1.5G efficiencies reaching 5.1%, a value approaching that of polymer solar cells that have seen two decades' investigation, conceptual advances, and optimization. The size-tunable bandgap, long carrier lifetime, and solution-processing are the three intrinsic advantages associated with lead chalcogenide CQD solar cells.

Table 3. Approximate estimation of device parameters to achieve the targeted efficiency for PbS CQD photovoltaic device [a].

Device efficiency	Device architecture	mobility ($cm^2 V^{-1} s^{-1}$)	N_A (cm^{-3})	$W_{depletion}$ (nm)	τ (μs)	$L_{diffusion}$ (nm)	V_{oc} (V)	J_{sc} (mA cm^{-2})	FF
~2% [b]	Schottky	10^{-5}~10^{-4}	~10^{17}	~100	~15	< 20	0.4	10	0.5
~5% [c]	p-n	10^{-4}~10^{-3}	~10^{16}	~200	~15	20 ~ 50	0.5	18	0.55
~10% [d]	p-n	10^{-3}~10^{-2}	~10^{15}	~800	~15	50 ~ 200	0.55	28	0.65

Notes: [a] All calculations are based on PbS CQDs with E_g ~ 1.3 eV; [b] Representative Schottky device performance based on PbS CQDs; [c] N_D in the n-type material is assumed to be ~ 10^{16} cm^{-3} and [d] N_D in the n-type material is assumed to be ~10^{18} cm^{-3}. Abbreviations: N_A acceptor density of CQD film; $W_{depletion}$ depletion region width in the CQD film; τ carrier lifetime; $L_{diffusion}$ carrier diffusion length.

We summarize in **Table 3** the electronic materials properties that will be required to advance CQD photovoltaics beyond 10% AM1.5G efficiency.

The key advances required are as follows:

1) Improve CQD surface engineering for enhanced electronic transport. Currently the carrier mobility in the best CQD photovoltaic devices has been of the order of 10^{-5}~10^{-3} cm^2 V^{-1} s^{-1}. An improvement of mobility to 10^{-2} $cm^2 V^{-1} s^{-1}$ and above will break the absorption-extraction tradeoff and lead to much improved J_{sc}. Previously-reported devices have had doping densities >10^{16} cm^{-3} and a further reduction in doping density to ~10^{15} cm^{-3} will increase the width of the high-IQE depletion region and promote carrier extraction. At a materials processing level, these advances require new strategies that simultaneously achieve excellent surface passivation combined with minimal interparticle spacing.
2) Improve device architectures. The move from Schottky to p-n heterojunction led to a doubling in solar efficiency, reinforcing the major impact of architecture on performance. n-i-p architectures exploiting wide-bandgap materials such as CdS, TiO_2, ZnO, SnO_2 and a-Si may offer further advances. Bulk heterojunctions and nanoporous electrodes and nanorod arrays offer to overcome in part present-day limitations in carrier mobility.
3) Improve CQD photovoltaic device stability further. Although the recent report of air stability of device is encouraging, further improvements in thermal stability require effort. Core/shell dots and recent progress in all-inorganic CQD films from molecular metal chalcogenide ligands may provide a path towards robustly-passivated quantum dot films exhibiting further-improved long-term stability.

Acknowledgements

This publication was based on work supported in part by Award No. KUS-I1-009-21, made by King Abdullah University of Science and Technology (KAUST). J.Tang thanks Dr. Ratan Debnath, Dr. Huan Liu, Dr. Xihua Wang and Steven Huang for their kind help during the course of manuscript preparation.

Received: April 23, 2010
Revised: June 15, 2010
Published online: September 14, 2010

[1] M. A. Green, K. Emery, Y. Hishikawa, W. Warta, *Prog. Photovoltaics* **2010**, *18*, 144.
[2] W. Guter, J. Schone, S. P. Philipps, M. Steiner, G. Siefer, A. Wekkeli, E. Welser, E. Oliva, A. W. Bett, F. Dimroth, *Appl. Phys. Lett.* **2009**, *94*.
[3] S. E. Shaheen, R. Radspinner, N. Peyghambarian, G. E. Jabbour, *Appl. Phys. Lett.* **2001**, *79*, 2996.
[4] H. Y. Chen, J. H. Hou, S. Q. Zhang, Y. Y. Liang, G. W. Yang, Y. Yang, L. P. Yu, Y. Wu, G. Li, *Nat. Photon.* **2009**, *3*, 649.
[5] M. C. Scharber, D. Wuhlbacher, M. Koppe, P. Denk, C. Waldauf, A. J. Heeger, C. L. Brabec, *Adv. Mater.* **2006**, *18*, 789.
[6] J. Tang, G. Konstantatos, S. Hinds, S. Myrskog, A. G. Pattantyus-Abraham, J. Clifford, E. H. Sargent, *ACS Nano* **2009**, *3*, 331.
[7] S. Maenosono, T. Okubo, Y. Yamaguchi, *J. Nanopart. Res.* **2003**, *5*, 5.
[8] H. M. Haverinen, R. A. Myllyla, G. E. Jabbour, *Appl. Phys. Lett.* **2009**, *94*.
[9] M. Singh, H. M. Haverinen, P. Dhagat, G. E. Jabbour, *Adv. Mater.* **2010**, *22*, 673.
[10] H. M. Haverinen, R. A. Myllyla, G. E. Jabbour, *J. Display Tech.* **2010**, *6*, 87.
[11] S. Coe-Sullivan, W. K. Woo, J. S. Steckel, M. Bawendi, V. Bulovic, *Org. Electron.* **2003**, *4*, 123.
[12] S. Coe, W. K. Woo, M. Bawendi, V. Bulovic, *Nature* **2002**, *420*, 800.
[13] J. L. Zhao, J. A. Bardecker, A. M. Munro, M. S. Liu, Y. H. Niu, I. K. Ding, J. D. Luo, B. Q. Chen, A. K. Y. Jen, D. S. Ginger, *Nano Lett.* **2006**, *6*, 463.
[14] H. Hoppe, N. Arnold, N. S. Sariciftci, D. Meissner, *Sol. Energy Mater. Sol. Cells* **2003**, *80*, 105.
[15] A. R. Denton, N. W. Ashcroft, *Phys. Rev. A* **1991**, *43*, 3161.
[16] L. E. Brus, *J. Chem. Phys.* **1983**, *79*, 5566.
[17] L. E. Brus, *J. Chem. Phys.* **1984**, *80*, 4403.
[18] M. A. Hines, G. D. Scholes, *Adv. Mater.* **2003**, *15*, 1844.
[19] E. H. Sargent, *Nature Photon.* **2009**, *3*, 325.
[20] Q. Q. Dai, Y. N. Wang, X. B. Li, Y. Zhang, D. J. Pellegrino, M. X. Zhao, B. Zou, J. Seo, Y. D. Wang, W. W. Yu, *ACS Nano* **2009**, *3*, 1518.
[21] I. Moreels, K. Lambert, D. Smeets, D. De Muynck, T. Nollet, J. C. Martins, F. Vanhaecke, A. Vantomme, C. Delerue, G. Allan, Z. Hens, *ACS Nano* **2009**, *3*, 3023.
[22] M. Law, M. C. Beard, S. Choi, J. M. Luther, M. C. Hanna, A. J. Nozik, *Nano Lett.* **2008**, *8*, 3904.
[23] J. P. Clifford, G. Konstantatos, K. W. Johnston, S. Hoogland, L. Levina, E. H. Sargent, *Nat. Nanotechnol.* **2009**, *4*, 40.
[24] K. W. Johnston, A. G. Pattantyus-Abraham, J. P. Clifford, S. H. Myrskog, S. Hoogland, H. Shukla, J. D. Klem, L. Levina, E. H. Sargent, *Appl. Phys. Lett.* **2008**, *92*.
[25] K. M. Coakley, M. D. McGehee, *Chem. Mater.* **2004**, *16*, 4533.
[26] B. Oregan, M. Gratzel, *Nature* **1991**, *353*, 737.
[27] W. J. Yoon, K. Y. Jung, J. W. Liu, T. Duraisamy, R. Revur, F. L. Teixeira, S. Sengupta, P. R. Berger, *Sol. Energy Mater. Sol. Cells* **2010**, *94*, 128.

[28] M. Redecker, D. D. C. Bradley, M. Inbasekaran, E. P. Woo, *Appl. Phys. Lett.* **1998**, *73*, 1565.
[29] G. Juska, M. Viliunas, K. Arlauskas, N. Nekrasas, N. Wyrsch, L. Feitknecht, *J. Appl. Phys.* **2001**, *89*, 4971.
[30] D. V. Talapin, J. S. Lee, M. V. Kovalenko, E. V. Shevchenko, *Chem. Rev.* **2010**, *110*, 389.
[31] D. V. Talapin, C. B. Murray, *Science* **2005**, *310*, 86.
[32] J. P. Clifford, K. W. Johnston, L. Levina, E. H. Sargent, *Appl. Phys. Lett.* **2007**, *91*.
[33] J. Tang, L. Brzozowski, D. A. R. Barkhouse, X. H. Wang, R. Debnath, R. Wolowiec, E. Palmiano, L. Levina, A. G. Pattantyus-Abraham, D. Jamakosmanovic, E. H. Sargent, *ACS Nano* **2010**, *4*, 869.
[34] R. Bose, J. F. McMillan, J. Gao, K. M. Rickey, C. J. Chen, D. V. Talapin, C. B. Murray, C. W. Wong, *Nano Lett.* **2008**, *8*, 2006.
[35] N. F. Mott, *Adv. Phys.* **1967**, *16*, 49.
[36] N. F. Mott, *Philos. Mag.* **1969**, *19*, 835.
[37] A. L. Efros, B. I. Shklovskii, *J. Phys. C: Solid State Phys.* **1975**, *8*, L49.
[38] A. L. Efros, B. I. Shklovskii, *Phys. Status Solid B* **1976**, *76*, 475.
[39] A. Zabet-Khosousi, A. A. Dhirani, *Chem. Rev.* **2008**, *108*, 4072.
[40] H. E. Romero, M. Drndic, *Phys. Rev. Lett.* **2005**, *95*, 156801.
[41] Y. Liu, M. Gibbs, J. Puthussery, S. Gaik, R. Ihly, H. W. Hillhouse, M. Law, *Nano Lett.* **2010**, *10*, 1960.
[42] S. A. McDonald, G. Konstantatos, S. G. Zhang, P. W. Cyr, E. J. D. Klem, L. Levina, E. H. Sargent, *Nat. Mater.* **2005**, *4*, 138.
[43] K. W. Johnston, A. G. Pattantyus-Abraham, J. P. Clifford, S. H. Myrskog, D. D. MacNeil, L. Levina, E. H. Sargent, *Appl. Phys. Lett.* **2008**, *92*.
[44] M. V. Kovalenko, M. Scheele, D. V. Talapin, *Science* **2009**, *324*, 1417.
[45] J. M. Luther, M. Law, M. C. Beard, Q. Song, M. O. Reese, R. J. Ellingson, A. J. Nozik, *Nano Lett.* **2008**, *8*, 3488.
[46] M. Law, J. M. Luther, O. Song, B. K. Hughes, C. L. Perkins, A. J. Nozik, *J. Am. Chem. Soc.* **2008**, *130*, 5974.
[47] E. J. D. Klem, H. Shukla, S. Hinds, D. D. MacNeil, L. Levina, E. H. Sargent, *Appl. Phys. Lett.* **2008**, *92*.
[48] J. M. Luther, M. Law, Q. Song, C. L. Perkins, M. C. Beard, A. J. Nozik, *ACS Nano* **2008**, *2*, 271.
[49] G. I. Koleilat, L. Levina, H. Shukla, S. H. Myrskog, S. Hinds, A. G. Pattantyus-Abraham, E. H. Sargent, *ACS Nano* **2008**, *2*, 833.
[50] J. E. Murphy, M. C. Beard, A. J. Nozik, *J. Phys. Chem. B* **2006**, *110*, 25455.
[51] M. C. Beard, A. G. Midgett, M. Law, O. E. Semonin, R. J. Ellingson, A. J. Nozik, *Nano Lett.* **2009**, *9*, 836.
[52] J. W. Stouwdam, F. van Veggel, *Langmuir* **2004**, *20*, 11763.
[53] A. J. Morris-Cohen, M. D. Donakowski, K. E. Knowles, E. A. Weiss, *J. Phys. Chem. C* **2010**, *114*, 897.
[54] G. Konstantatos, L. Levina, A. Fischer, E. H. Sargent, *Nano Lett.* **2008**, *8*, 1446.
[55] D. A. R. Barkhouse, A. G. Pattantyus-Abraham, L. Levina, E. H. Sargent, *ACS Nano* **2008**, *2*, 2356.
[56] L. Turyanska, U. Elfurawi, M. Li, M. W. Fay, N. R. Thomas, S. Mann, J. H. Blokland, P. C. M. Christianen, A. Patane, *Nanotechnology* **2009**, *20*.
[57] J. Aldana, Y. A. Wang, X. G. Peng, *J. Am. Chem. Soc.* **2001**, *123*, 8844.
[58] I. Moreels, B. Fritzinger, J. C. Martins, Z. Hens, *J. Am. Chem. Soc.* **2008**, *130*, 15081.
[59] N. B. Pendyala, K. Rao, *J. Lumines.* **2008**, *128*, 1826.
[60] M. A. Hines, P. Guyot-Sionnest, *J. Phys. Chem.* **1996**, *100*, 468.
[61] M. Fernee, A. Watt, J. Warner, J. Riches, N. Heckenberg, H. Rubinsztein-Dunlop, *J. Cryst. Growth* **2004**, *270*, 380.
[62] M. J. Fernee, A. Watt, J. Warner, S. Cooper, N. Heckenberg, H. Rubinsztein-Dunlop, *Nanotechnology* **2003**, *14*, 991.
[63] A. C. Bartnik, F. W. Wise, A. Kigel, E. Lifshitz, *Phys. Rev. B* **2007**, *75*.
[64] M. Brumer, A. Kigel, L. Amirav, A. Sashchiuk, O. Solomesch, N. Tessler, E. Lifshitz, *Adv. Funct. Mater.* **2005**, *15*, 1111.
[65] D. V. Talapin, H. Yu, E. V. Shevchenko, A. Lobo, C. B. Murray, *J. Phys. Chem. C* **2007**, *111*, 14049.
[66] J. M. Pietryga, D. J. Werder, D. J. Williams, J. L. Casson, R. D. Schaller, V. I. Klimov, J. A. Hollingsworth, *J. Am. Chem. Soc.* **2008**, *130*, 4879.
[67] E. Lifshitz, M. Brumer, A. Kigel, A. Sashchiuk, M. Bashouti, M. Sirota, E. Galun, Z. Burshtein, A. Q. Le Quang, I. Ledoux-Rak, J. Zyss, *J. Phys. Chem. B* **2006**, *110*, 25356.
[68] G. M. Dalpian, J. R. Chelikowsky, *Phys. Rev. Lett.* **2006**, *96*.
[69] S. C. Erwin, L. J. Zu, M. I. Haftel, A. L. Efros, T. A. Kennedy, D. J. Norris, *Nature* **2005**, *436*, 91.
[70] J. J. Urban, D. V. Talapin, E. V. Shevchenko, C. R. Kagan, C. B. Murray, *Nat. Mater.* **2007**, *6*, 115.
[71] D. K. Ko, J. J. Urban, C. B. Murray, *Nano Lett.* **2010**, *10*, 1842.
[72] A. C. Sharma, *J. Appl. Phys.* **2006**, *100*.
[73] J. J. Choi, Y. F. Lim, M. B. Santiago-Berrios, M. Oh, B. R. Hyun, L. F. Sung, A. C. Bartnik, A. Goedhart, G. G. Malliaras, H. D. Abruna, F. W. Wise, T. Hanrath, *Nano Lett.* **2009**, *9*, 3749.
[74] J. Nelson, *The Physics of Solar Cells*, World Scientific Pub Co. Inc., **2003**.
[75] W. Ma, J. M. Luther, H. M. Zheng, Y. Wu, A. P. Alivisatos, *Nano Lett.* **2009**, *9*, 1699.
[76] R. Debnath, J. Tang, D. A. Barkhouse, X. H. Wang, A. G. Pattantyus-Abraham, L. Brzozowski, L. Levina, E. H. Sargent, *J. Am. Chem. Soc.* **2010**, *132*, 5952.
[77] A. G. Pattantyus-Abraham, I. Kramer, A. R. Barkhouse, X. Wang, G. Konstantatos, R. Debnath, L. Levina, I. Raabe, M. K. Nazeeruddin, M. Gratzel, E. H. Sargent, *ACS Nano* **2010**, *18*, 144.
[78] P. R. Yu, K. Zhu, A. G. Norman, S. Ferrere, A. J. Frank, A. J. Nozik, *J. Phys. Chem. B* **2006**, *110*, 25451.
[79] S. Gunes, H. Neugebauer, N. S. Sariciftci, H. Roither, M. Kovalenko, G. Pillwein, W. Heiss, *Adv. Funct. Mater.* **2006**, *16*, 1095.
[80] D. Dissanayake, R. A. Hatton, T. Lutz, R. J. Curry, S. R. P. Silva, *Nanotechnology* **2009**, *20*, 5.
[81] S. W. Tsang, H. Fu, R. Wang, J. Lu, K. Yu, Y. Tao, *Appl. Phys. Lett.* **2009**, *95*.
[82] B. Sun, A. T. Findikoglu, M. Sykora, D. J. Werder, V. I. Klimov, *Nano Lett.* **2009**, *9*, 1235.
[83] K. S. Leschkies, T. J. Beatty, M. S. Kang, D. J. Norris, E. S. Aydil, *ACS Nano* **2009**, *3*, 3638.
[84] J. Tang, X. H. Wang, L. Brzozowski, D. A. R. Barkhouse, R. Debnath, L. Levina, E. H. Sargent, *Adv. Mater.* **2010**, *22*, 1398.
[85] G. Konstantatos, E. H. Sargent, *Appl. Phys. Lett.* **2007**, *91*.
[86] K. P. Fritz, S. Guenes, J. Luther, S. Kumar, N. S. Sariciftci, G. D. Scholes, *J. Photochem. Photobiol. A-Chem.* **2008**, *195*, 39.
[87] A. Stavrinadis, J. M. Smith, C. A. Cattley, A. G. Cook, P. S. Grant, A. A. R. Watt, *Nanotechnology* **2010**, *21*, 185202.
[88] S. Kitada, E. Kikuchi, A. Ohno, S. Aramaki, S. Maenosono, *Solid State Commun.* **2009**, *149*, 1853.
[89] Z. N. Tan, T. Zhu, M. Thein, S. A. Gao, A. Cheng, F. Zhang, C. F. Zhang, H. P. Su, J. K. Wang, R. Henderson, J. I. Hahm, Y. P. Yang, J. Xu, *Appl. Phys. Lett.* **2009**, *95*.
[90] Y. Y. Feng, D. Q. Yun, X. Q. Zhang, W. Feng, *Appl. Phys. Lett.* **2010**, *96*.
[91] S. J. Kim, W. J. Kim, A. N. Cartwright, P. N. Prasad, *Sol. Energy Mater. Sol. Cells* **2009**, *93*, 657.